BSGF - Earth Sciences Bulletin 2025, 196, 13
© C. Passos do Carmo *et al.*, Published by EDP Sciences 2025
https://doi.org/10.1051/bsgf/2025004

Available online at:
www.bsgf.fr

Petrogenetic link between metasedimentary rocks, migmatites and granitoids in the Variscan basement of the Pontgibaud area, French Massif Central – implications for the crustal structure

Caliméria Passos do Carmo[1,*], Olivier Vanderhaeghe[1], Oscar Laurent[1], Julien Berger[1], Mathieu Bellanger[2], Mathieu Leisen[1] and Jérôme Chmeleff[1]

[1] Géosciences Environnement Toulouse, CNRS, IRD, UT3, Observatoire Midi-Pyrénées, 14 av. E. Belin, 31400 Toulouse, France
[2] TLS Geothermics

Received: 10 November 2023 / Accepted: 1 March 2025 / Publishing online: 18 July 2025

Abstract – The architecture of the crust in the French Massif Central (FMC) is described as a nappe stack composed, from top to bottom, of the Upper Gneiss Unit (UGU), the Lower Gneiss Unit (LGU), and the Para-Autochthonous Unit (PAU), which are intruded by Carboniferous granitic plutons. In the Pontgibaud region, the Upper Gneiss Unit/Lower Gneiss Unit (UGU/LGU) attribution and the relationship between metamorphic and magmatic rocks are uncertain. This hinders both our understanding of the geodynamic processes that led to the construction of the Variscan orogenic belt, and a precise assessment of the deep geothermal potential of this high-heat flow area. Our field investigations document a metamorphic gradient with, from South to North, micaschists and paragneiss with a gently, dominantly southward–dipping foliation grading into migmatites that display a steeper foliation. A maximum late Ediacaran deposition age of sedimentary protoliths is determined from LA-ICPMS U–Pb dates of the youngest detrital zircon populations that range from 588.9 ± 7.1 to 571.8 ± 8.2 Ma. Equilibrium phase diagrams calculated for selected samples document a metamorphic gradient from 2.3– 5.3 kbar, and 570°–660°C, characterizing a mid- to low pressure-high temperature event dated from 357.6 ± 1.5 to 342.2 ± 4.6 Ma by LA-ICP-MS U–Pb analyses of metamorphic monazite. The contact between the metasedimentary rocks and migmatites is crosscut by peraluminous, cordierite-biotite-bearing Claveix and Gelles granitic plutons dated at 338.0 ± 7.3 Ma and 323.3 ± 9.7 Ma, respectively by U–Pb on zircon. The distribution of U–Pb dates and Lu–Hf isotopic compositions of detrital zircon in metamorphic rocks; the absence of HP mineral relics; the age of HT metamorphism of *ca.* 357–345 Ma; and the lack of a major mylonitic tectonic contact, which would typify the base of UGU, collectively support that the exposed crust of the Pontgibaud area corresponds to LGU metamorphic rocks. Moreover, the mineralogy, bulk chemistry and zircon Lu–Hf isotopic composition of the granites and migmatites are consistent with an origin by partial melting of LGU metasedimentary rocks. These data show that the Pontgibaud area exposes a section along a Carboniferous MP-LP/HT metamorphic gradient from micaschists to migmatites. Genesis and extraction of a large volume of granitic magma require higher temperatures (>800 °C) that were not reached by the exposed rocks. Accordingly, we propose that the local mid- and lower crustal levels are made of rocks with a similar protolith as those exposed at the surface, but affected by higher metamorphic grade and magma extraction.

Keywords: French Massif Central / Variscan belt / migmatites / crustal structure / metamorphism

Résumé – Lien pétrogénétique entre roches métasédimentaires, migmatites et granitoïdes dans le socle varisque de la région de Pontgibaud, Massif Central Français - implications pour la structure crustale. L'architecture de la croûte dans le Massif central français (FMC) est décrite comme un empilement de nappes composé, de haut en bas, de l'unité supérieure de gneiss (USG), de l'unité inférieure de gneiss (UIG) et de l'unité para-autochtone (UPA), qui sont intrudées par des plutons granitiques du Carbonifère. Dans la région de Pontgibaud, l'attribution USG/UIG et la relation entre les roches métamorphiques et magmatiques sont incertaines. Cela limite à la fois notre compréhension des processus géodynamiques qui ont conduit à la construction de la ceinture orogénique varisque, et une évaluation précise du potentiel

---

*Corresponding author: calimeria.carmo@get.omp.eu

géothermique profond de cette zone à flux de chaleur élevé. Nos résultats de terrain documentent un gradient métamorphique avec, du sud au nord, des micaschistes et des paragneiss avec une foliation légèrement inclinée vers le sud, passant à des metatexites et diatexites avec une foliation plus pentée. L'âge maximum de dépôt des protolithes sédimentaires à la fin est déterminé à partir des âges U–Pb obtenus par LA-ICP-MS avec des populations de zircons détritiques qui vont de 588.9 ± 7.1 à 571.8 ± 8.2 Ma. La modélisation thermodynamique des échantillons sélectionnés donne des conditions de 2.3 à 5.3 kbar et de 570° à 660°C, caractérisant un événement de basse pression-haute température daté par U–Pb (LA-ICP-MS) sur monazite métamorphique entre 357.6 ± 1.5 et 342.2 ± 4.6 Ma. Les roches métamorphiques sont intrudées, par les plutons granitiques peralumineux de Claveix et de Gelles, des granites à cordiérite et biotite, datés respectivement à 338.0 ± 7.3 Ma et à 323.3 ± 9.7 Ma par des analyses U–Pb sur zircon.

La distribution des âges U–Pb et des compositions isotopiques Lu–Hf du zircon détritique dans les roches métamorphiques, l'absence de reliques minérales HP, l'âge du métamorphisme HT d'environ 357-345 Ma et l'absence d'une structure majeure reconnue, qui caractériserait la base de l'USG, confirment collectivement que les micaschistes, les paragneiss et les gneiss migmatitiques de la région de Pontgibaud correspondent à l'UIG. De plus, la minéralogie, la chimie en roche totale et la composition isotopique Lu–Hf des zircons des granites sont compatibles avec une origine des roches plutoniques par fusion partielle des roches métasédimentaires de l'UIG. En conséquence, ces données montrent que la région de Pontgibaud expose une section le long d'un gradient métamorphique LP/HT du Carbonifère, allant des micaschistes aux migmatites. La genèse et l'extraction d'un grand volume de magma granitique nécessitent des températures plus élevées (>800°C) qui n'ont pas été atteintes par les roches exposées. Nous proposons donc que les roches métamorphiques locales de la croûte moyenne et inférieure ont un protolithe similaire à celui des roches exposées à la surface, mais de caractère résiduel après extraction de melt, et affecté par un grade métamorphique supérieur.

Mots-clés : Massif Central Français / chaîne varisque / migmatites / structure crustale / metamorphisme

1 Introduction

Orogenic processes, and in particular partial melting of the deep crust, extraction of granitic magmas therefrom and their transfer to higher crustal levels, play a crucial role in the differentiation of the continental crust (Brown, 2001; Vanderhaeghe and Teyssier, 2001; Vanderhaeghe, 2009; Hawkesworth *et al.*, 2010; Sawyer *et al.*, 2011; Cawood *et al.*, 2013; Moyen *et al.*, 2017). In turn, these processes control the vertical distribution of the heat-producing elements K, U and Th and thus influence the thermal state of the crust over tens of million years (England and Thompson 1984; Sandiford *et al.*, 2002).

The nature of the lower crust is ill–defined relative to the one of the upper crust (Rudnick, 1995; Hacker *et al.*, 2011). Its architecture can nevertheless be deciphered from the structural, petrological, geochemical and geochronological analysis of exhumed metamorphic and plutonic rocks that are representative of crustal roots.

The Variscan Belt of Western Europe formed during the convergence between Gondwana and Laurussia in the late Paleozoic and resulted in the assembly of the Pangea supercontinent (Matte, 2001). In most areas of the Variscan Belt, tectonic accretion and continental collision were responsible for crustal thickening followed by thermal relaxation and/or lithospheric thinning, which triggered widespread partial melting of the orogenic root (Burg and Vanderhaeghe, 1993; Henk *et al.*, 2000; Vanderhaeghe and Teyssier, 2001). This led to a voluminous magmatic event with contribution from both crustal and mantle sources (Finger *et al.*, 1997; Janoušek *et al.*, 2000; Laurent *et al.*, 2017; Moyen *et al.*, 2017; Jacob *et al.*, 2021).

The French Massif Central (FMC) is part of the internal zone of the Variscan Belt (referred to as the Moldanubian Domain; (Ballèvre *et al.*, 2014; Lardeaux *et al.*, 2014) and records different stages of the orogenic evolution (from subduction to collision; (Matte 1986; Ledru *et al.*, 1989; Lardeaux *et al.*, 2001; Faure *et al.*, 2009). The exposure in the FMC mainly consists of metasedimentary and meta-igneous-metasedimentary rocks affected by metamorphism from greenschist to upper amphibolite or even granulite facies (up to partial melting conditions), and abundant granitic plutons. Metamorphic rocks were mainly exhumed to the surface during the Carboniferous and thus correspond to the former upper and mid–Crust of the Variscan basement of Western Europe. Direct information on mid to lower Variscan crustal levels is accessible in parts of the Variscan Belt such as the Ivrea-Verbano Zone (Brodie *et al.*, 1982; Zingg *et al.*, 1990; Demarchi *et al.*, 1998; Barboza *et al.*, 1999; Handy *et al.*, 1999) and the Pyrenees (Vielzeuf 1996; Olivier *et al.*, 2008; Guille *et al.*, 2019; Vielzeuf *et al.*, 2021).

However, in the case of the FMC, information on the lower crust is accessible only through xenoliths sampled during Cenozoic volcansism, which are overall rare, unevenly distributed across the FMC (Leyreloup *et al.*, 1977; Dostal *et al.*, 1980; Downes and Leyreloup 1986; Leyreloup 1992; Costa and Rey 1995; Laurent *et al.*, 2023), and do not allow to investigate the relationships between exposed lithological units and lower crustal rocks. As a result, the deep architecture of the continental crust in the FMC is still debated (see Vanderhaeghe *et al.*, 2020 for a review).

A nappe stack comprised of an Upper Gneiss Unit (UGU), a Lower Gneiss Unit (LGU), and a Para-Autochthonous Unit (PAU) has been recognised in the Eastern part of the FMC (Burg and Matte, 1978; Ledru *et al.*, 1989) and has been refined in the Western part with the addition of an intermediate allochthon (Girardeau *et al.*, 1986; Berger *et al.*, 2010). The reconstruction of this nappe stack has been based on the recognition of mylonitic contacts and of inverted metamorphic gradients (Burg *et al.*, 1984; Burg *et al.*, 1989). Several propositions have also been made regarding the nature of the crust beneath these nappes and the uncertainty to that respect is expressed in the “unknown Proterozoic basement” invoked by Faure *et al.*, (2009). In the first crustal-scale model, (Matte 1986) proposed that the thrusts separating the nappes are rooted in the Moho, eluding the presence of migmatites exposed at the lowest structural level. In contrast, other authors proposed that migmatites coring crustal-scale domes such as the Velay dome, represent a partially molten crust that was exhumed during gravitational collapse of the orogenic crust (Gardien *et al.*, 1990; Burg and Vanderhaeghe, 1993; Costa and Rey 1995; Ledru *et al.*, 2001; Bouilhol *et al.*, 2006; Gardien *et al.*, 2011). The comparison of data from the FMC’s xenoliths with exposed sections of the Variscan crust in the Pyrenees and in the Alps served to propose that the lower crust beneath the migmatites is composed of a combination of felsic and mafic granulites that might correspond to a residue left after extraction of magmas from the partially molten orogenic root, associated with some mantle–Derived magmas and/or pre-Variscan mafic igneous rocks (Dostal *et al.*, 1980; Vielzeuf *et al.*, 1990; Costa and Rey, 1995; Vanderhaeghe, 2009; Laurent *et al.*, 2023).

In the Pontgibaud region, the attribution of tectono-metamorphic units and the relationship between metamorphic and plutonic rocks are uncertain. This is exemplified by discrepancies, at the scale of the 1/50 000 scale geological map of Pontgibaud (Hottin *et al.*, 1989) and the 1M geological map of France (Chantraine *et al.*, 2003), in the attribution of the migmatitic gneisses exposed in the northern part of the studied area. This is of particular interest since the area has been identified as a potential target for deep geothermal energy production (Duwiquet *et al.*, 2019; Duwiquet *et al.*, 2021). Indeed, the potential for deep geothermal requires reconstructing the geothermal gradient as precisely as possible, which relies in part on the vertical distribution of heat-producing elements and thus on a model for the crustal-scale architecture. In order to fill this knowledge gap and improve the assessment of the geothermal potential of the Variscan crust of the FMC, the goal of this study is to characterise the Variscan geological record (structure, P–T–t–d -–Dhistory, magmatic transfers) of the Pontgibaud area using structural analysis, conventional petrography, phase equilibria modelling, bulk-rock geochemistry and U–Pb geochronology and isotopic analyses on accessory minerals.

2 Geological

2.1 Geology of the FMC

The FMC is part of the late Paleozoic Variscan orogenic belt that resulted of convergence between the supercontinents Gondwana and Laurussia, as well as the intervening crustal blocks Avalonia and Armorica, to form the Pangea supercontinent (Matte 2001). The FMC represents the inverted northern Gondwana margin (Lardeaux *et al.*, 2014; Chelle-Michou *et al.*, 2017; Couzinié *et al.*, 2019). It was originally described as a stack of litho-tectonic nappes showing an inverted metamorphic gradient (Burg *et al.*, 1984). Hereafter, we only describe the three main units, relevant for the investigated area. These units are from top to bottom and roughly from North to South (Burg and Matte, 1978; Ledru *et al.*, 1989; Santallier *et al.*, 1994; Faure *et al.*, 2008; Lardeaux *et al.*, 2014):

- The Upper Gneiss Unit (UGU) is composed of migmatitic gneiss and metasedimentary rocks that underwent Devonian eclogitic–Granulitic HP –HT metamorphism followed by early Carboniferous (360–350 Ma) HT retrogression into amphibolite facies (Gardien *et al.*, 2011; Benmammar *et al.*, 2020). This unit contains the so–Called Leptyno–Amphibolite Complex (LAC) that is interpreted to represent bimodal magmatic rocks with relicts of HP to UHP (eclogite–Facies) Silurian to Devonian metamorphism (Pin and Lancelot, 1982; Santallier *et al.*, 1988; Gardien *et al.*, 1990; Santallier *et al.*, 1994; Lardeaux *et al.*, 2001);
- The Lower Gneiss Unit (LGU) consists of metasedimentary and metaigneous rocks affected by lower Carboniferous amphibolite–Facies metamorphism characteristic of MP–MT conditions with a pressure peak at 350–340 Ma, followed by upper Carboniferous (330–300 Ma) HT metamorphism (Schulz *et al.*, 1996; Mougeot *et al.*, 1997; Schulz 2009; Schulz 2014; Do Couto *et al.*, 2016; Chelle-Michou *et al.*, 2017);
- The Para-autochthonous Unit (PAU) is made of metasedimentary and rare metaigneous rocks of usually greenschist-to lower amphibolite–Facies metamorphism that are overthrusted by the LGU and UGU units.

Both the UGU and LGU largely consist of Neoproterozoic to early Paleozoic (Cambrian–Ordovician) metasedimentary rocks and orthogneisses. Deposition of the precursor sedimentary sequences likely took place from the Ediacaran to the early Paleozoic (Melleton *et al.*, 2010; Couzinié *et al.*, 2019). The Lu–Hf signature of detrital zircons indicates that these sequences were fed by erosion of both the cratonic basement of northern Gondwana and juvenile Neoproterozoic terranes including the Arabian–Nubian shield and/or the Cadomian arc (Chelle-Michou *et al.*, 2017; Couzinié *et al.*, 2019; Avigad *et al.*, 2022). Metasedimentary units are associated with former granites and minor mafic rocks of Ediacaran–Cambrian to Ordovician age, transformed into orthogneisses (Chelle-Michou *et al.*, 2017; Couzinié *et al.*, 2017; Lardeaux *et al.*, 2014; Melleton *et al.*, 2010) or alternate with the Leptyno-Amphibolite Complex. These meta-igneous rocks are described as products of two main igneous events at *ca.* 540 and *ca.* 480 Ma, respectively related to (i) inversion of an Ediacaran back-arc basin formed between the Cadomian arc and the northern Gondwana margin (Couzinié *et al.*, 2017; 2019); and (ii) extension related to the opening of the Medio–Europeanpaleo-ocean and drift of the Armorica block from the Gondwana margin (Pin and Lancelot, 1982; Faure *et al.*, 2009; Lardeaux *et al.*, 2014; Chelle-Michou *et al.*, 2017)). Markers of ocean closure by subduction are eclogites, blueschists and calc-alkaline plutons and rare volcanics (Berger *et al.*, 2024). In the French Massif central, HP pressure metamorphism has been first documented to have occurred between Silurian and Early Devonian ((Pin and Lancelot, 1982); see also Lardeaux, 2014 and references therein) but recent dating in southern FMC yielded Upper Devonian to Lowermost Carboniferous ages for eclogitic metamorphism (Lotout *et al.*, 2018; Lotout *et al.*, 2020). This is in agreement with the magmatic record, in particular the various expressions of calc-alkaline active margin magmatism that also occurred during the Upper Devonian, especially in the Limousin area in the western FMC (Bernard–Griffiths and Cornichet, 1985; Shaw *et al.*, 1993; Bertrand *et al.*, 2001; Pin and Paquette, 2002).

In the case of the FMC the production of large amounts of granitic magma is attested by the widespread exposition of migmatites and granitic bodies showing zircon crystallization ages from approximately 360 Ma to 290 Ma (see compilation in Vanderhaeghe *et al.*, 2020, and references therein). The magmatic activity in this interval is characterised by melting of dominantly crustal sources (represented by pre –Variscan, both metasedimentary and metaigneous rocks), leading to emplacement of dominantly peraluminous, S-type granites (see Moyen *et al.*, 2017) and references therein). In the eastern part of the FMC (*i.e.,* east of the Sillon Houiller strike-slip fault; Fig. 1), crustal melting resulted in the development of the large (*ca.* 100 km in diameter) Velay granite-migmatite dome (Burg and Vanderhaeghe, 1993; Barbey *et al.*, 1999, 2015; Ledru *et al.*, 2001) and is accompanied by significant contribution of lithospheric mantle sources, as shown by the coeval emplacement of peraluminous granites and "vaugnerites" (Mg–K rich lamprophyres) and associated granitoids from *ca.* 350 to 300 Ma (von Raumer *et al.*, 2014; Couzinié *et al.*, 2016; Laurent *et al.*, 2017; Moyen *et al.*, 2017; Werle *et al.*, 2023).

2.2 Pontgibaud geology

The Pontgibaud region is located in the Eastern French Massif Central (in relation to the Sillon Houiller fault zone), between the Sioule, Artense and Haut-Allier regions, which are type localities where the UGU/LGU relationships have been previously established (Fig.1B–C). The Pontgibaud area is bounded by the Sillon Houiller sinistral fault zone to the West and the Aigueperse-St-Sauves fault zone to the East. The geological map of the studied area was established based on the work of (Fernandez, 1969; Tempier, 1969; Tempier, 1974; Fernandez and Tempier, 1977; Négroni, 1981), and the geological map of Hottin *et al* (1989). The main metamorphic lithological units are, from S to N (i) aluminous micaschists comprised of alternating quartz–feldspar rich metyagrauwacke and aluminosilicate-rich metapelite; (ii) biotite + sillimanite ± muscovite paragneisses, locally containing garnet; (iii) minor and poorly exposed, quartzo–feldspathic orthogneisses; (iv) metatexitic paragneiss, represented by biotite ± cordierite ± garnet ± sillimanite; and (iv) cordierite diatexite.

The structural record of the studied area has been documented (Fernandez, 1969; Tempier, 1974; Fernandez and Tempier, 1977; Négroni 1981). These data are synthesised in the 1/50 000 scale geological map of Pontgibaud (Hottin *et al.*, 1989). Following these authors and our own field observations, micaschists and paragneiss display a shallow–dipping foliation, associated with rootles isoclinal folds that are correlated with kilometre scale isoclinal folds with NE–SW striking axes plunging dominantly to the SW. This foliation is affected by three generations of open upright folds with, in chronological order, E–W, NW–SE, and N-S striking axial planes, the latter being preferentially expressed to the NW of the Gelles pluton. In the migmatites, the foliation is steeply dipping to vertical and its direction displays a chaotic pattern on the map scale.

Metamorphic rocks are intruded by biotite ± cordierite- and muscovite-bearing Variscan granitic plutons, namely the Claveix fine–Grained granite, forming an intrusive body feeding a *ca.* 6 km-long N–S trending porphyritic dyke; and the Gelles porphyritic granite, forming a *ca.* 12 x 6 km pluton associated with volumetrically minor, satellite granite porphyry dykes. Based on field relationships, the Gelles granite is interpreted as intrusive in the Claveix granite (Fernandez and Tempier, 1977; Hottin *et al.*, 1989). The detailed analysis of the Gelles pluton served to develop the structural analysis of granitoids based on the preferred orientation of feldspar megacrysts (Fernandez, 1969; Fernandez and Tempier, 1977). The magmatic foliation, depicted by the preferred orientation of feldspar megacrysts and by microgranular enclaves, shows a roughly concentric distribution, parallel to the contacts of the oval-shaped pluton. The northern and southern margins of the plutons are steeply dipping. The western contact of the pluton with the metamorphic hosts is gently dipping toward the West, whereas the eastern contact is steeply dipping toward the East. The lineation marked by the preferred orientation of the long axis of feldspar megacrysts is shallowly dipping towards the West in the western part of the pluton and is steeply dipping towards the East in the eastern part.

In early works (Fernandez, 1969; Tempier, 1974; Fernandez and Tempier, 1977; Négroni, 1981) the micaschists and paragneiss of the southern part of the studied area were represented structurally on top of the sillimanite- and cordierite-bearing migmatites, and this transition was interpreted as a metamorphic gradient. This proposition has been subsequently challenged by tentative correlations of the different litho-tectonic units to the nappe structure of the French Massif Central, but the attribution of these units to either UGU or LGU is still unclear. In the 1/50 000e map, the attribution of the metamorphic rocks to the LGU or UGU has essentially been made based on the presence of amphibolite lenses in the migmatitic gneisses; and correlations with rocks exposed in the Artense dome further SW (Hottin *et al.*, 1989). Accordingly, the micaschists are attributed to the LGU, the migmatites to the UGU and the paragneisses to a third metamorphic unit referred to as "Undifferentiated Gneiss Unit" (Hottin *et al.*, 1989). In contrast, on the geological map of France at the 1:1 000 000/ scale (Chantraine *et al.*, 2003), the paragneisses are attributed to either the LGU to the west of the Gelles Granite, or to the UGU to the southeast (Chantraine *et al.*, 2003) (see dashed black line in Fig.1C).

3 Materials and Methods

Following field studies and preliminary petrographic investigation on a set of 30 samples, eight of them were selected for further investigation, as representatives of the main identified lithological units in the Pontgibaud area: one micaschist (PG21-04), two paragneisses (PG20-01 and PG21-28), two metatexitic paragneisses (PG20-02 and PG21-20, sampled at the same locality), one diatexite (PG20-4), one sample of porphyritic-texture Claveix granite along the N-S trending dyke (PG20-05), and one sample of

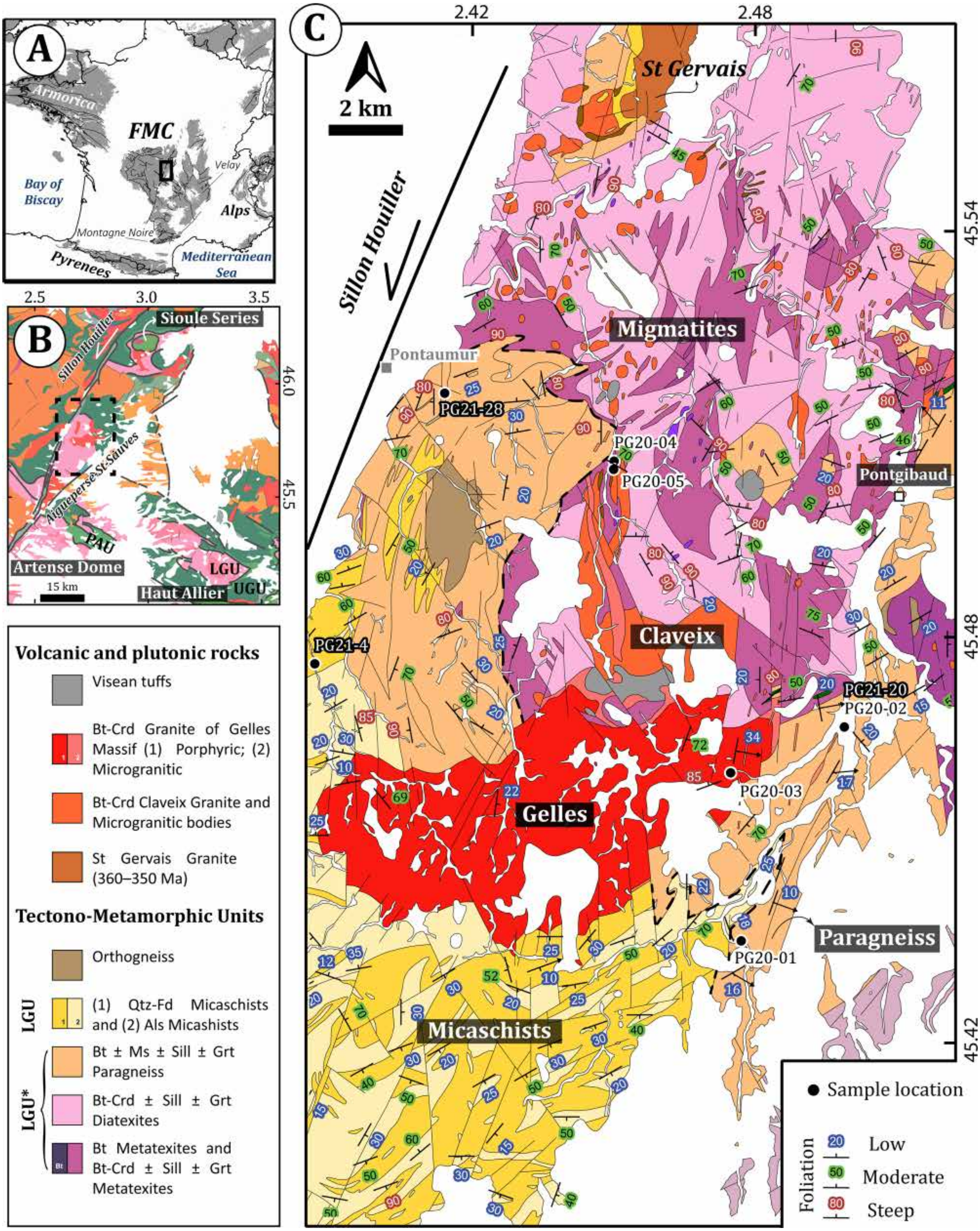

Fig. 1. (a) General context of the French Massif Central. (b) Sketch map of the Variscan basement of the Pontgibaud region showing the spatial distribution of LGU, UGU and PAU units, and localities where these nappes were defined (Sioule Series, Artense Dome and Haut Allier). Modified after Chantraine *et al.*, (2003). (c) Geological map of the Pontgibaud region. The dashed black line represents the UGU/LGU contact proposed by Chantraine *et al.* (2003). Note that paragneiss are either attributed to LGU (north-west of Gelles granite) or UGU (south-east of Gelles granite). Modified after Hottin *et al.*, (1989).

Table 1. Bulk rock composition in oxide weight per cent for the samples collected in this study. Locations of samples are shown in Figure 1.

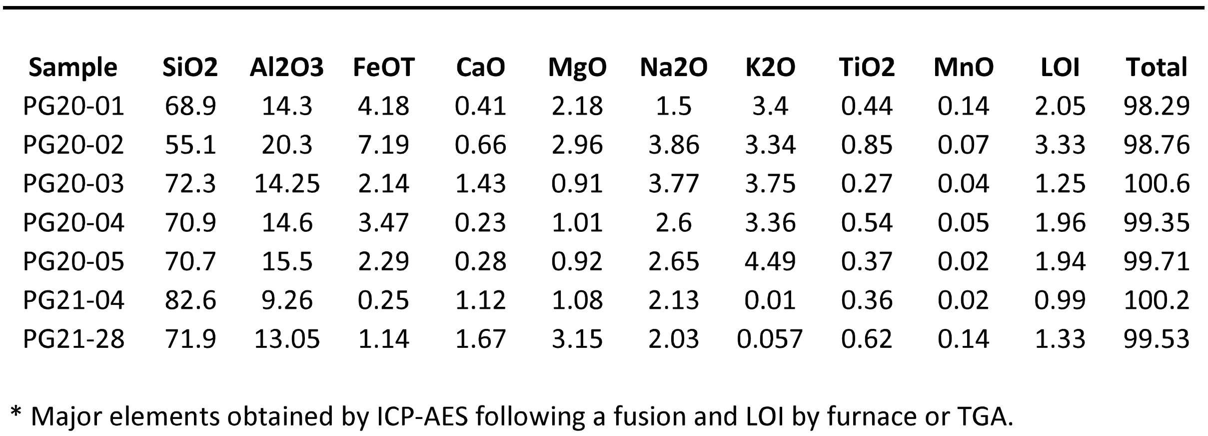

Sample	SiO2	Al2O3	FeOT	CaO	MgO	Na2O	K2O	TiO2	MnO	LOI	Total
PG20-01	68.9	14.3	4.18	0.41	2.18	1.5	3.4	0.44	0.14	2.05	98.29
PG20-02	55.1	20.3	7.19	0.66	2.96	3.86	3.34	0.85	0.07	3.33	98.76
PG20-03	72.3	14.25	2.14	1.43	0.91	3.77	3.75	0.27	0.04	1.25	100.6
PG20-04	70.9	14.6	3.47	0.23	1.01	2.6	3.36	0.54	0.05	1.96	99.35
PG20-05	70.7	15.5	2.29	0.28	0.92	2.65	4.49	0.37	0.02	1.94	99.71
PG21-04	82.6	9.26	0.25	1.12	1.08	2.13	0.01	0.36	0.02	0.99	100.2
PG21-28	71.9	13.05	1.14	1.67	3.15	2.03	0.057	0.62	0.14	1.33	99.53

* Major elements obtained by ICP-AES following a fusion and LOI by furnace or TGA.

Gelles granite (PG20-03). Sample locations are reported in Figure 1.

Sample preparation was performed at the Géosciences Environnement Toulouse - Observatoire Midi-Pyrénées (GET-OMP) laboratory, France. Rock samples were sawed to prepare 30 µm-thick petrographic thin sections and, for some of them, *ca.* 50 µm-thick sections for i-N-S itu monazite geochronology by LA-ICP-MS. The samples were reduced and subsequently crushed using a steel jaw crusher and a disc mill (all samples except PG21-28 paragneiss), a fraction of each sample was further crushed to a sub-µm fraction in an agate swing mill for whole rock major and trace elements analysis. Major elements compositions are shown in the pseudosection equilibrium diagrams (Figs. 12–13) ; complete data and ALS analytical procedure are reported in supplementary material and in Table 1.

3.1 Pseudosection calculation

The sub-µm rock powders were sent to ALS Global Geochemistry for whole-rock analysis, using conventional ICP-OES (for major elements) and ICP-MS (for trace elements) analysis following alkali fusion and wet acid digestion of the samples. The results were used as representative of bulk sample compositions for thermodynamic modelling.

Pseudosection calculations combined with thin section observation and major–Element analyses of main mineral phases were performed in order to obtain the metamorphic P–T conditions recorded by the samples. Major element analysis on feldspar, muscovite, biotite and garnet were performed using an CAMECA SXFive electron microprobe at the Centre de Microcaractérisation Raimond Castaing in Toulouse, France, in order compare the mineral compositions with calculated mineral isopleths. Analytical conditions were an acceleration voltage of 15 kV, a beam current of 10 nA for the micas and 20 nA for garnet and feldspar, and, a spot size of 2 µm.

Phase diagrams and isopleths were calculated using Perple_X software (Connolly 2009) with thermodynamic databases and mineral compositions from Holland & Powell, (2011), using the 9–Components system SiO_2–Al_2O_3—FeO–MnO–MgO–Na_2O—CaO–K_2O–TiO_2. The water content was set at saturation for modelling. Ferric iron is not included in the model due to the lack of major phases containing $Fe+^{3+}$. Solution models used for modelling are: muscovite (Coggon and Holland, 2002; Auzanneau *et al.*, 2009), biotite (Tajčmanová *et al.*, 2009), feldspar (Newton *et al.*, 1980; Holland and Powell, 2003), garnet (White *et al.*, 2000), chlorite (Holland *et al.*, 1998), sanidine (Waldbaum and Thompson, 1968), ilmenite (White *et al.*, 2000), cordierite (ideal), staurolite (Holland *et al.*, 1998), orthopyroxene (Holland and Powell, 1996), and melt (White *et al.*, 2001). The whole-rock compositions and representative mineral compositions are reported in the supplementary material and in Tables 1 and 2.

3.2 U-(Th-)–Pb geochronology

3.2.1 Zircon

Zircon separation was performed from the <500 µm sample fractions using standard heavy mineral concentration techniques (Wilfley shaking table, manual panning, Frantz magnetic separator and heavy liquids when necessary). The concentrated zircons were then hand-picked using a binocular microscope, set in 1-inch epoxy resin mounts and polished to a sub–Equatorial section. Attention was given to selecting zircons of different shapes and sizes in order to obtain representative zircons for each sample, especially for the populations of detrital grains in metasedimentary rocks.

The internal structures of the zircons were characterised using the Tescan rainbow cathodoluminescence (CL) detector attached to the Tescan Vega4 Scanning Electron Microscope (SEM) at GET. Conditions were an acceleration voltage of 10 kV and beam current of 3 nA.

Simultaneous analyses of U–Pb isotopes in zircons were conducted by laser ablation– inductively coupled plasma–mass spectrometry (LA-ICP-MS) at the Service ICP-MS of Observatoire Midi-Pyrénées (OMP-UAR831). The analyses were carried using a NWRfemto (Elemental Scientific Instruments) solid-state femtosecond laser ablation system set to UV mode (257 nm wavelength) coupled with an Element XR (ThermoScientific) sector–Field ICP-MS. Measurements were performed with a laser spot diameter

Table 2. Representative mineral compositions in oxide weight per cent for biotite, muscovite, plagioclase and garnet.

	Biotite				Muscovite		Plagioclase				Garnet	
Sample	**PG20-01**	**PG20-02**	**PG21-04**	**PG21-28**	**PG20-01**	**PG21-04**	**PG20-01**	**PG20-02**	**PG21-04**	**PG21-28**	**PG21-28**	
Texture	**matrix**	**matrix**	**matrix**	**matrix**	**inclusio**	**matrix**	**matrix**	**matrix**	**matrix**	**matrix**	rim	core
Na_2O	0.07	0.28	0.33	0.13	0.46	1.14	10.35	10.84	10.67	9.21	0.04	0
Al_2O_3	18.63	18.45	19.66	19.45	35.02	35.90	21.74	20.94	21.33	23.03	20.89	20.77
SiO_2	35.13	34.86	35.58	34.63	46.51	45.86	64.54	65.48	66.37	62.95	36.91	36.96
K_2O	9.39	8.63	8.75	9.67	10.38	9.39	0.15	0.33	0.14	0.16	0.01	0
MnO	0.18	0.14	0.13	0.33	0.05	0.02	0.03	0.04	0.00	0.03	10.89	9.89
FeO	18.39	18.76	18.61	18.23	0.90	0.76	0.08	0.00	0.01	0.03	26.98	27.21
MgO	8.55	8.31	9.51	9.01	0.80	0.56	0.04	0.00	0.00	0.00	3.12	3.21
TiO_2	3.26	3.67	2.01	2.54	0.75	0.64	0.00	0.00	0.00	0.00	0	0
CaO	0.00	0.00	0.00	0.00	0.00	0.00	2.82	1.82	1.90	4.12	0.79	0.87
Total	93.71	93.83	95.09	94.65	95.08	94.88	99.74	99.52	100.43	99.53	99.64	98.92
XMn											0.26	0.29
XFe	0.55	0.56	0.52	0.53							0.60	0.53
XMg	0.45	0.44	0.48	0.47							0.12	0.15
XCa							12.98	8.34	8.92	19.73	0.03	0.03
Si					3.10	3.06						

of 20 µm, a repetition rate of 6 Hz and an energy density of *ca.* 2.5 J/cm^2. Ablation was performed in the built-in, dual-volume, fast-washout ablation cell (<1 cm^3 effective volume) flushed with He carrier gas (*ca.* 0.6 L/min) to which was admixed Ar make-up gas (*ca.* 0.88 L/min) downstream of the ablation cell before introduction in the plasma. A typical run consisted of 30 seconds of background signal acquisition, followed by 30 seconds of ablation and 10 seconds of washout. The list of acquired masses, corresponding dwell times, details about the instrument optimization and data acquisition procedures are provided in the Supplementary Table X.

The resulting intensities were processed offline with the Igor Pro Iolite v2.5 software (Hellstrom *et al.*, 2008), using the VizualAge data reduction scheme (Petrus and Kamber, 2012) for U–Pb dating. The GJ1 zircon reference material (using isotope ratios from (Horstwood *et al.*, 2016) was used as primary standard for correction of instrumental drift, mass bias and laser-induced U/Pb fractionation (following (Paton *et al.*, 2010)) through conventional standard-sample bracketing (Hellstrom *et al.*, 2008). Secondary zircon standards Plešovice (Sláma *et al.*, 2008), Mud Tank (Horstwood *et al.*, 2016) and AUSZ7-1 (Kennedy *et al.*, 2014) were analyzed as unknowns to confirm the accuracy of the results. The obtained U–Pb ages for all secondary standards (see Supplementary Table 1) are accurate within the total bulk reproducibility of the method, which is ~2 per cent relative (2σ) (Horstwood *et al.*, 2016). The data from unknowns and reference materials are provided in Supplementary Table X. Results were plotted in Concordia diagrams and Concordia or Discordia ages were calculated whenever possible, using the IsoplotR online package (Vermeesch, 2018). For age calculations, data treatment was performed as proposed by (Spencer *et al.*, 2016) through outlier rejection as to obtain a suitable MSWD based on the constraints from (Wendt and Carl, 1991). Systematic uncertainties were propagated in the uncertainties of pooled ages (*i.e.* calculated from the average of several individual data points) as recommended by Horstwood *et al.*, (2016).

3.2.2 Monazite

In situ U–Pb dating of monazite was performed directly in thin sections of paragneiss PG20-01, metatexitic paragneiss PG20-02; and diatexite PG20-04. Monazites in thin sections were imaged using the same SEM instrument as mentioned above in backscattered electron (BSE) mode and with X-ray maps.

For U–Pb isotopic analyses, the same LA-ICP-MS system as mentioned for zircon U–Pb dating was used, with the same analytical conditions except for a 7 µm spot size and timing parameters of 20 seconds background signal acquisition, 20 seconds of ablation and 10 seconds of washout delay. Data processing was performed using the same software and procedures as for zircon U–Pb dating, using the Moacyr monazite reference material (using isotope ratios from Gasquet *et al.*, (2010) as primary standard and Manangoutry (Paquette and Tiepolo, 2007) as secondary standard. Details about the analytical conditions and results on the secondary reference material are provided in the Supplementary Table Y.

3.3 Zircon Lu-Hf isotopes

Zircon Lu–Hf isotopic analysis were performed by laser ablation– multi–Collection– inductively coupled plasma–mass spectrometry (LA-MC-ICP-MS) at OMP. A high-resolution MC-ICP-MS Neptune Plus (Thermo Scientific) was coupled to the same femtosecond laser ablation system as used for U–Pb geochronology. Analyses were performed on some selected zircons, in the same spot locations as previously dated with the U–Pb technique or within the same growth zone, and attention was given to select zircons with >90 per cent of concordance and representative of all groups of ages. The ablation, aerosol transport and timing parameters were the same as for zircon U–Pb measurements, except for a 50 μm spot diameter and repetition rate of 7 Hz. More details about the analytical parameters are reported in Supplementary Table X.

The data were processed offline with the Igor Pro-based Iolite v2.5 software, using an in-house data reduction scheme. Instrumental mass bias for Yb and Hf isotopes were corrected to the natural abundance ratios ^{173} Yb/^{171}Yb and ^{179} Hf/^{177}Hf of Chu *et al.*, (2002). Mass bias for Lu isotopes was assumed identical to that for Yb isotopes. The isobaric interferences of ^{176} Yb and ^{176} Lu on ^{176} Hf were corrected using the natural abundance ratios of ^{176} Yb/^{173}Yb = 0.79502 and ^{176} Lu/^{175}Lu = 0.02656. The Yb- and Lu-poor zircon reference material Mud Tank (Woodhead and Hergt, 2005) was used as primary reference material to correct for instrumental drift and any offset on the interference–Corrected ^{176} Hf/^{177}Hf ratios (generally not exceeding 1 to 2 εHf-units). Accuracy and external reproducibility of the method were controlled by repeated analyses of reference zircon standards 91500 (Wiedenbeck *et al.*, 1995), GJ-1 (Morel *et al.*, 2008), Maniitsoq (Marsh *et al.*, 2019), Plešovice (Slamá *et al.*, 2008) and Temora (Woodhead and Hergt, 2005). The ^{176} Hf/^{177}Hf ratios obtained on all reference materials are within uncertainties identical to the recommended values (see Supplementary Table X). Calculations of initial ^{176} Hf/^{177}Hf ratios and εHf were performed using a ^{176} Lu decay constant of 1.865×10^{-11} (Scherer *et al.*, 2001) and ^{176} Hf/^{177}Hf and ^{176} Lu/^{177}Hf values for the chondritic uniform reservoir (CHUR) recommended by (Bouvier *et al.*, 2008).

4 Results

4.1 Field Observations

Our field observations confirm that the metamorphic units in the Pontgibaud region, as described in Tempier (1969; 1974) and Hottin *et al.*, (1989), are dominated by metasedimentary rocks that correspond to alternation of quartz–Feldspar rich and aluminosilicate rich micaschists that progressively grade into paragneiss migmatites towards the North (Fig. 2). In the following, we present outcrop-scale features of these rocks and describe their regional-scale structural relationships. In the map of figure 2, the structural measurements correspond to the ones reported by Tempier, (1974) and Hottin, (1989) for the metamorphic rocks and by Négroni (1981) and Fernandez, (1969) for the Gelles pluton, complemented with our own data. Note that in previously published maps, the authors did not distinguish the different generations of structures, and the structural symbols correspond to dominant structure identified at the outcrop scale. The representation on the cross sections of the different generations of structures relies on our outcrop scale observations and on the correlations with previously published structural measurements. A detailed description of the mineral assemblage and texture of the studied samples is provided in the next section.

The micaschists and paragneisses, which enclose rare, km-scale lenses of fine–Grained orthogneiss with a granitic composition, are located on a topographic high, to the South of the Gelles pluton. Outcrops are generally variably weathered road cuts and small quarries. Metasediments are composed essentially of quartz, plagioclase, and biotite, differing in the presence of andalusite and higher content of muscovite in the micaschist, whereas the paragneiss contains sillimanite with rare garnet. At the outcrop scale, the alternation of coarse–Grained, quartz-rich layers and fine–Grained, mica-rich layers is interpreted to represent the former sedimentary bedding (Fig. 3B). This bedding is transposed into a major sub-horizontal $S/_{0/n}$ foliation, also marked by the preferred orientation of micas, which are in an axial planar position of rootless isoclinal folds identified in the field (Figs. 2, 3B) and described by Tempier (1974). The isoclinal folds display a dominant NE–SW trending axis and associated with the development of a discrete axial planar schistosity $S+_{n+1}$ (Fig. 3A–B). This main foliation is trending roughly parallel to lithological contacts that delineate an arch-shape from a preferred NE–SW to E–W orientation to the East of the Gelles pluton and scattered around a - N-S direction in the paragneiss domain to the West of the pluton (Fig. 1). The main foliation is also transposed into NW-SE-trending subvertical upright folds in the western part of the studied area, close to the Sillon Houiller and into an E–W trending subvertical schistosity in an axial planar position of upright folds, more markedly toward the transition with the migmatites.

The micaschists and paragneisses to the south of the Gelles pluton, grade into migmatites that form the bulk of the exposure in the northern part of the studied area (Fig. 1). The transition from micaschists to migmatites occurs progressively over a couple kilometers and is marked, from South to North by the succession of metatexites and diatexites with a gradual increase of leucosome proportions. Migmatite outcrops are generally relatively small, discontinuous and variably weathered road cuts, such that the relationships with other lithologies are difficult to establish. The metatexitic paragneiss, which only corresponds to a kilometre-thick zone between paragneiss and diatexite, is characterised by the alternation of centimetre to decimetre thick leucosome and mesosome layers, which delineate a synmigmatitic foliation. Leucosome veins concordant to the foliation are in textural continuity with veins discordant to the foliation (Fig. 3C–D), pointing to syntectonic melt segregation and magma migration at the grain to outcrop scales. Diatexites are dominated by a granite with a heterogeneous texture and containing abundant cordierite as well as numerous enclaves of metatexitic paragneiss (Fig. 3–E).

Along the southern margin of the migmatites, the synmigmatitic foliation of the metatexitic paragneiss displays roughly the same strike as the $S/_{0/n}$ foliation of the micaschists and paragneisses but is in general steeper (Fig. 2). In contrast, the orientation of the synmigmatitic foliation of the diatexites, defined by dismembered schlieren and restitic enclaves in the

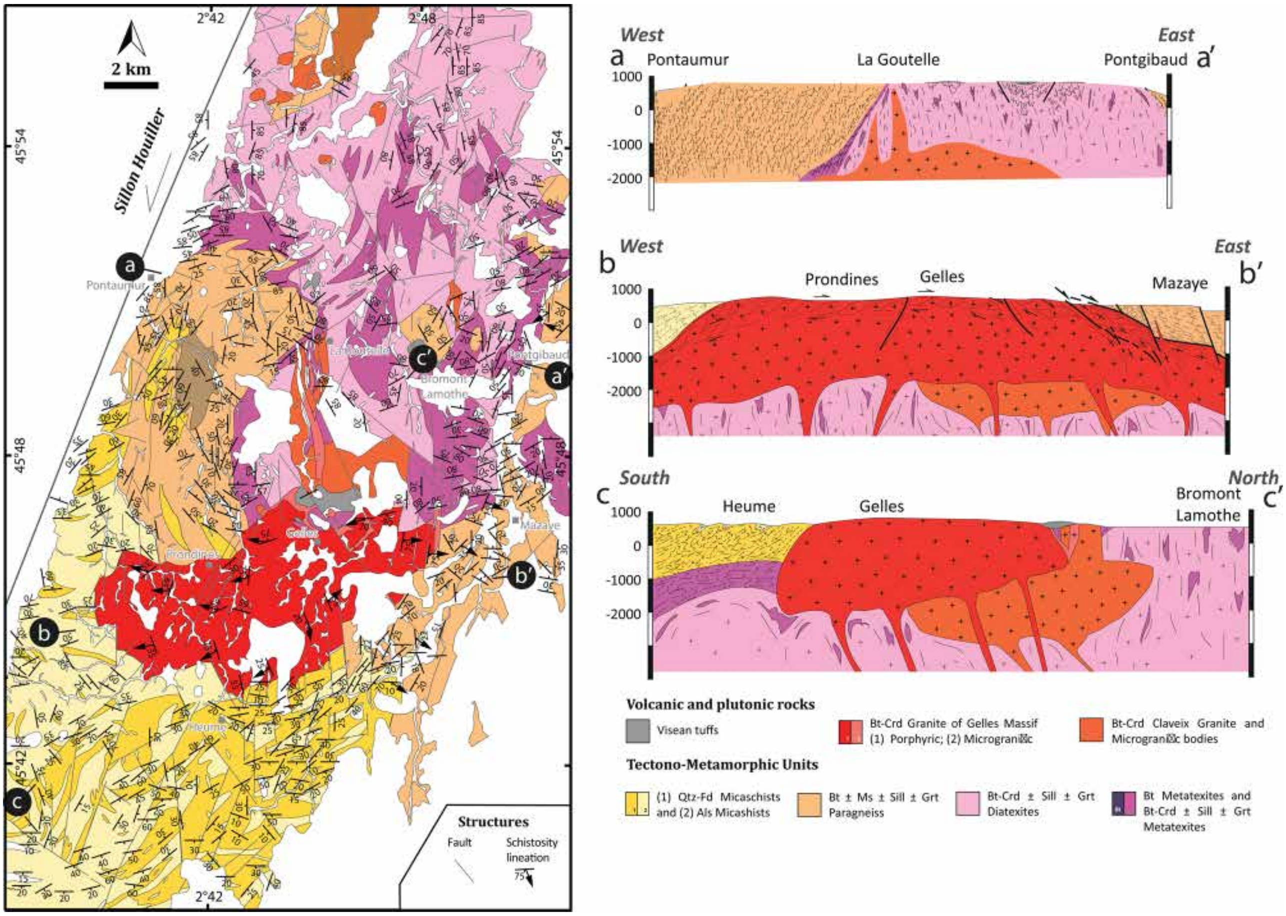

Fig. 2. Interpretative cross-sections (locations of the profiles are shown in Fig. 1c) showing relationships between micaschist, paragneiss, migmatites and plutonic rocks, and structural observations.

granitic matrix, is more heterogeneous and does not display a preferred orientation. The synmigmatitic foliation in both, metatexite and diatexite, is generally concordant to lithological contacts, possibly delineating in kilometre scale subdomes within the migmatites (Fig. 3C).

The metamorphic rocks are intruded by the Claveix and Gelles granitic plutons, which crosscut the roughly E–W trending contact between the micaschist-paragneiss series and the migmatites (Fig. 1 and 2). The main body of the Claveix granite (Hottin *et al.*, 1989) consists of homogeneous, equigranular, two-mica- and cordierite-bearing granite, which is poorly exposed. It grades to the north into a broad, N-S directed dyke associated with porphyry-like granite bodies with sub-volcanic textures (Figs. 2 and 3F). Locally, the dyke clearly crosscuts the foliation of migmatites and shows a chilled margin with quartz and feldspar phenocrysts enclosed in a very fine–Grained groundmass (Fig. 3F). The Gelles pluton forms a low-topography flat zone in which isolated exposures are generally strongly weathered, whereas fresh outcrops are mainly restricted to the pluton's margins, especially to the east along the escarpment of the Sioule valley. Granite forming the core of the pluton is a coarse–Grained, porphyritic biotite–Cordierite- and minor muscovite-bearing granite containing K–Feldspar phenocrysts up to 5 cm long (Fig. 3 G-H). Tourmaline may be present as a disseminated mineral (Hottin, 1989) or, together with quartz, as veinlets cross–Cutting the granite. The Gelles pluton is dominated by a shallow–Dipping magmatic fabric underlined by the preferred orientation of K–Feldspars phenocrysts. Along the western contact of the Gelles pluton, this magmatic fabric is shallowly dipping toward the West and displays an E–W trending preferred orientation of the long axis of K–Feldspar phenocrysts. These phenocrysts locally display bookshelf docking and are affected by ductile deformation marked by a C/S fabric consistent with a top to the East sense of shear (Fig. 2 and 3G). Along the eastern contact, the magmatic fabric is dipping to the East and is crosscut by mylonitic to cataclastic shear zones steeply dipping to the East that are running parallel to the N-S trending faults indicated on the map (Fig. 2). The shear direction is indicated by the stretching direction of quartz and feldspar in mylonite and by mechanical striaes in cataclasite. Deflection of the ductile fabric into these shear zones is consistent with a top to the East sense of shear.

4.2 Petrography

4.2.1 Micaschists and paragneiss

Sample PG21-04 is representative of the micaschists located to the SW of the study area, composed of mostly

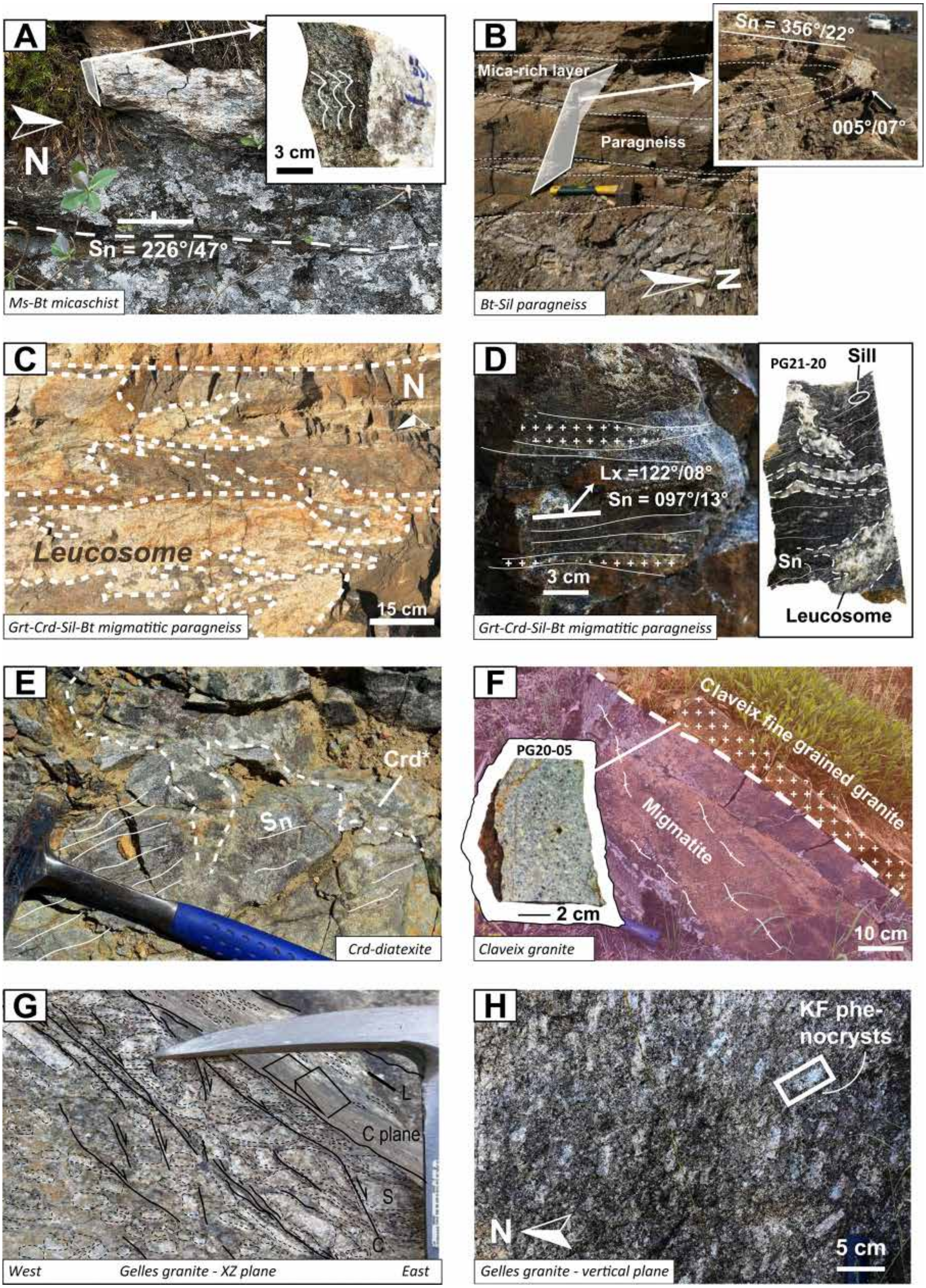

Fig. 3. Outcrop features of (A) Ms–Bt micaschist and macroscopic sample (inset) affected by crenulation folding with N–S trending axes; the observation plane of the macroscopic sample is marked in white. (B–D) Bt–Sil paragneiss affected by an isoclinal fold (B), and displaying concordant to discordant leucosomes (C, D). (E) Migmatite outcrop displaying foliated metatexite crosscut by Crd-bearing diatexite. (F) Migmatite and Claveix granite discordant contact, inset showing a macroscopic sample of the granite. (G–H) Gelles granite exhibiting (G) C–S fabric and (H) oriented K-feldspar phenocrysts in a vertical plane (pink pencil as scale). Structural measurements are reported in dip direction/dip.

biotite, muscovite, quartz and plagioclase with an alternation of mica-rich and quartz -rich layers (Fig. 4A). Andalusite is the main index metamorphic mineral and is localised in the mica-rich layers. It is present as sub-idioblastic crystals oriented parallel to the main foliation and containing inclusions of muscovite and biotite (Fig. 4B). Quartz-rich layers present polygonal grain boundaries attesting for grain boundary migration during solid-state recrystallization. Accessory minerals comprise rutile, ilmenite, tourmaline, apatite, zircon and monazite. Mica-rich layers contain centimeter-sized round and fractured porphyroclasts porphyroblasts (possibly cordierite, see below), completely transformed in sericite. These porphyroclasts contain inclusion of white mica and ilmenite that delineate a schistosity continuous to the one of the matrix but they are also wrapped into the foliation, which points to their syntectonic crystallization. Similar pseudomorphosed porphyroclasts have been previously interpreted as cordierite described in this area (Hottin *et al.*, 1989). Biotite contains inclusions of zircon, monazite and rutile. Ilmenite is present as small crystals in the matrix and as sub-idioblastic to xenoblastic crystals enclosed in the porphyroblasts. Some ilmenite inclusions reach a length up to 200 μm and contain quartz inclusions.

Paragneisses PG20-01, PG21-28 and metatexitic paragneiss PG20-02 present a paragenesis composed of plagioclase + biotite ± K–Feldspar ± sillimanite ± garnet together with accessory zircon, monazite and apatite. The main foliation in all samples is marked by the preferred orientation of biotite. A network of concordant to discordant leucosome veins points to syntectonic melt segregation. In sample PG20-01 sillimanite occurs as fibrolite aggregates mostly concordant to the main foliation, usually embedded in a fine–Grained quartz–muscovite matrix (Fig. 4D) suggesting the retrograde metamorphic reaction:

K–Feldspar + sillimanite + biotite → muscovite + quartz

Sillimanite aggregates are either concordant with, folded in, or overprinting the foliation, which suggests that deformation occurred in the stability field of sillimanite. The K–Feldspar and plagioclase crystals are respectively rounded and elongated, and contain numerous quartz, biotite and more rarely muscovite inclusions. K–Feldspar and plagioclase form aggregates that are wrapped into mica-rich layers marking the main foliation forming a symmetric sigma-type shape pointing to syn-kinematic recrystallization. Chlorite is locally replacing biotite, and, along with rutile, is more common in the leucosome. As documented in the micaschists, the sample contains porphyroclasts, presumably cordierite pseudomorphs, totally altered to white mica (Hottin *et al.*, 1989). Leucosome veins contain tabular and skeletal muscovite replacing sericitised idioblastic minerals (presumably cordierite), and rarely relics of sillimanite. Quartz of leucosome veins displays serrated to lobate grain boundaries typical of dynamic recrystallisation by bulging and grain boundary migration (GBM).

Sample PG21-28, at northwest of the studied area, is a fine–Grained garnet-biotite-plagioclase-quartz paragneiss with a lepidoblastic texture defined by the orientation of biotite. Xenoblastic to sub-idioblastic crystals of garnet occur typically in biotite-rich domains, frequently as atoll crystals (Fig. 4E). Garnet crystals, when not as atoll texture, comprise an inclusion-rich core and an inclusion-poor rim. The inclusions consist mostly of quartz and apatite, rarely biotite, muscovite and rutile. Smaller square-shape inclusions, analysed by EDS, typically present C and O peaks pointing either to organic matter or to decrepitated fluid inclusions. Rare fibrolite and mica flakes are interlayered with biotite.

4.2.2 Metatexitic paragneiss

Metatexitic paragneiss sample PG20-02 resembles PG20-01 in mineralogy. They are characterised by a synmigmatitic foliation delineated by the alternation of mesosome and concordant leucosome veins. The mesosoma has a granoblastic texture and is made of tabular crystals of plagioclase, quartz, biotite and sillimanite aggregates. Sillimanite is also present as inclusions in the core of plagioclase crystals. Early muscovite also occurs in this sample as inclusion in biotite or plagioclase. The texture of the metatexitic paragneiss PG20-02 is characterised by rounded porphyroclasts and interstitial quartz films interpreted as a former melt phase wetting the grains. Concordant leucosome veins are composed mainly of quartz associated to plagioclase and K–Feldspar, they are folded and boudinaged. Quartz grains are characterised by polygonal boundaries that attest for high-temperature recrystallization. Pseudomorphosed porphyroclasts are replaced by sericite and fine–Grained acicular crystals of sillimanite (Fig. 4C). These porphyroclasts are wrapped into the main foliation, are surrounded by pressure shadows and contain helicitic inclusions indicating a syntectonic growth (Fig. 4C).

4.2.3 Diatexites

Sample PG20-04 is a diatexite composed of quartz, plagioclase, K–Feldspar, biotite, muscovite, cordierite, and chlorite together with accessory zircon, monazite, apatite and rutile. Its texture is heterogeneous and the granitic matrix contains enclaves of metatexites. At the microscopic scale the matrix is either made of equigranular euhedral plagioclase and K–Feldspar crystals with interstitial quartz, or of poikilitic K–Feldspar containing plagioclase inclusions (Fig. 4F). Polycrystalline domains with quartz present chessboard microstructure and ubiquitous serrated grain boundaries are indicative of solid-state deformation at high temperature. Enclaves of metatexites consist of biotite, sillimanite, plagioclase and quartz and display a metamorphic foliation. A pervasive alteration is marked by transformation of feldspars, cordierite, and sillimanite in micas.

4.3 Plutonic rocks

4.3.1 Claveix pluton

The main body of the Claveix pluton is described as an equigranular, fine-grained cordierite and biotite-bearing granite containing late muscovite. The sample PG20-05, investigated for U–Pb geochronology, was sampled NW of the Gelles pluton, in a body of porphyry-like granite associated with the Claveix granite (Fig. 1) near the contact with migmatites. It is a fine–Grained granite with feldspar crystals up to 2 mm (10 per cent) embedded in a fine–Grained feldspar + quartz darker matrix, defining a sub-volcanic texture. It is composed of plagioclase, K–Feldspar, quartz and minor chloritised biotite (Fig. 4G). Accessory minerals are zircon and apatite. Feldspars are euhedral, whereas quartz is sub–Euhedral to anhedral/skeletal.

4.3.2 Gelles pluton

The predominant facies of the Gelles pluton is a granite exposed in the centre of the studied area straddling the contact between migmatites and metasedimentary rocks. At the mesoscale, it is a leucocratic granite characterised by a porphyritic-textured, defined by K–Feldspar phenocrysts (20 per cent) in a matrix that consists of plagioclase (30 per cent), K–Feldspar (20 per cent), quartz (30 per cent) and biotite (Fig. 4H) with, more rarely, cordierite, muscovite and tourmaline. Plagioclase often display inclusion-rich cores. Accessory minerals are zircon and apatite. Tabular K–Feldspar phenocrysts are up to 3 cm size, often presenting oriented fabric defining a dominantly subhorizontal magmatic fabric.

4.3.3 Chemistry of the Claveix and Gelles granitic plutons

Whole-rock bulk compositions obtained in this study for Claveix and Gelles granites samples along with data available in Hottin *et al.*, (1989) (n = 5 for Claveix granite and n = 7 for Gelles granite), plot in the field of peraluminous granites, ranging in composition from A/CNK (molar $Al_2O_3/[CaO+Na_2O+K_2O]$) ~ 1.11–1.3 and A/NK (molar $Al_2O_3/[Na_2O+K_2O]$) ~ 1.4-1.6. Both granites display similar concentrations of SiO_2(ranging from 69–74 wt. per cent), K_2O (~4 wt. per cent), Al_2O_3 (~15 wt. per cent) and CaO (~1 wt. per cent). They slightly differ in terms of FeO_T + MgO contents (3.21 wt. per cent for Claveix and 3.05 wt. per cent for Gelles, see Table 1). In diagrams such as A/CNK *vs.* A/NK and Na_2O+K_2O *vs.* SiO_2 the samples from this study and the ones compiled in Hottin *et al.*, (1989) yield values within the Variscan S-type granites (Couzinié *et al.*, 2017; Moyen *et al.*, 2017).

4.4 Mineral Chemistry

The compositional characteristics of the main minerals are presented in Fig. 5 and summarised below.

4.4.1 Plagioclase (Fig. 5A)

All metamorphic samples present plagioclase composition below 20 mol. per cent anorthite content (molar ratio Ca/[Ca+Na]). The composition of plagioclase in metatexitic paragneiss sample PG20-02 (~8 mol. per cent An) is intermediate between the ones of plagioclase in paragneiss PG20-01 (~ 12 mol. per cent An) and in diatexite PG20-04 (~ 2 mol. per cent An).

4.4.2 Muscovite (Fig. 5B)

The composition of muscovite in all samples displays between 3.02 and 3.12 cations of Si per formula unit (a.p.f.u., calculated in the basis of 11 Oxygen atoms) and Fe+Mg in a range between 0.08 and 0.14 cations a.p.f.u. The Fe+Mg content of sericite in the porphyroclasts in sample PG20-02 is higher (0.15– 0.18 cations a.p.f.u.) and may reflect the influence of the composition of the pseudomorphosed porphyroclast (presumably cordierite). Muscovite inclusions in plagioclase from paragneiss (PG20-01) present higher values of Si up to 3.2 cations (a.p.f.u.).

4.4.3 Biotite (Fig. 5C–D)

Biotite compositions from micaschist PG21-04 and paragneiss PG21-28 present the highest values of XMg (molar ratio $Mg/[Mg+Fe^{2+}]$) of 0.48-0.50 and the lowest values of Ti (between 0.10 and 0.12 cation a.p.f.u., calculated in the basis of 11 Oxygen atoms) of all analysed samples. Biotites from diatexite PG20-04 show lower values of XMg (*ca.* 0.3) and higher values of Ti (between 0.2 and 0.25 cation a.p.f.u.) than those of the other samples. Si content in biotite does not seems to vary and is approximatively 2.5 cations a.p.f.u. for all samples.

4.4.4 Garnet (Fig. 5E)

Garnet crystals from the investigated samples are typically almandine (>57 mol. per cent) in composition. Electronic microprobe profiles of selected crystals show a significant Mn zonation with X_{sSp} values ranging from 20 mol. per cent in the core to 30 mol. per cent in the rim and less important zonations of XAlm (from 57 to 61 mol. per cent respectively) and X_{Pyp} (from 10 to 13 mol. per cent respectively). Grossular content never exceeds 3 mol. per cent, rendering GASP estimations not reliable as mentioned by Holdaway (2001).

4.5 U-Pb–Pb dating on zircon

4.5.1 Zircons textures

Cathodoluminescence images of representative zircon grains of each sample are presented in Figure 6 along with spot location of U–Pb and Lu–Hf analysis. Zircons in micaschist (PG21-04), paragneiss (PG20-01), metatexitic paragneiss (PG20-02) and diatexite (PG20-04) samples are typically rounded and vary in size from 50 to 200 µm, with a few grains up to 200 µm in the diatexite. The zircon grains typically show a -Core–rim zonation internal texture, characterised by truncation of the core zoning pattern by the rim. The cores are generally oscillatory or sector zoned and CL-brighter than the rims. These general features do not apply to all grains and in particular, the core/rim volume ratio is very variable from a grain to another.

Zircons from the Claveix-related porphyritic granite (PG20-05) and of the Gelles granite -(PG20-03) are euhedral, usually prismatic, especially in PG20-03. Zircons from PG20-05 present oscillatory zoning in most crystals. Some of them show a distinct euhedral light interface between a dark rounded core and an oscillatory zoned mantle, as represented by zircon V-23 in Figure 6. Zircons in sample PG20-03 show more complex -Core–rim zonation relationships than in PG20-05, although with commonly oscillatory-zoned, CL-brighter cores and CL–Darker rims showing faint or no zoning.

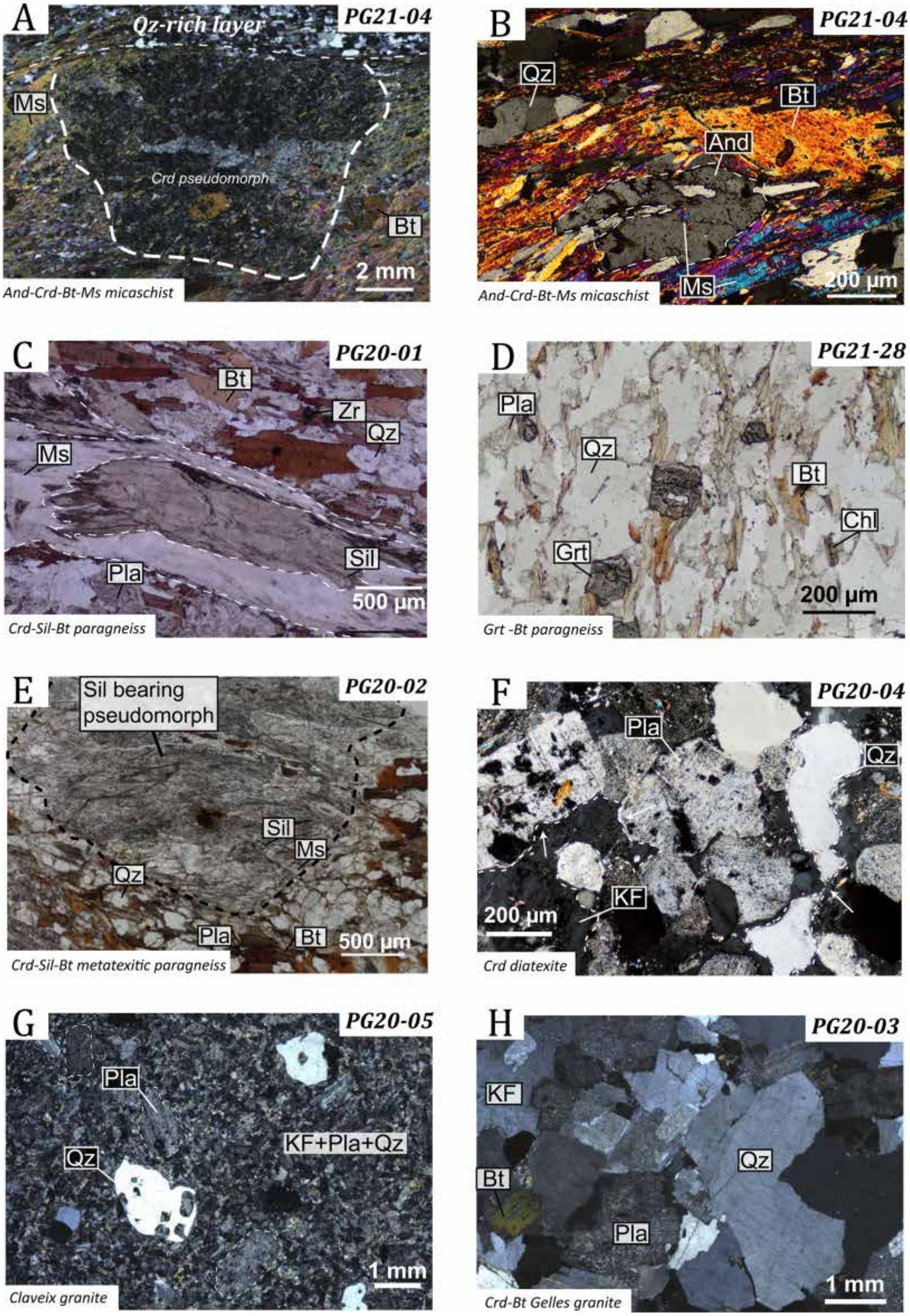

Fig. 4. Photomicrographs of (A–B) micaschist PG21-04: (A) in cross-polarised light (XPL), showing a pseudomorph, presumably after cordierite; (B) andalusite occurrence parallel to the main foliation. (C) Bt–Sil paragneiss PG20-01 in plane-polarised light (PPL), showing replacement of sillimanite by muscovite. (D) Grt–Bt paragneiss in PPL, showing garnets with inclusion-rich cores oriented along foliation. (E) Bt–Sil metatexitic paragneiss PG20-02, exhibiting a pseudomorphed crystal (probably Crd) replaced by sillimanite + muscovite. (F) Crd–bearing diatexite sample PG20-04, showing poikiloblastic texture of K-feldspar enclosing plagioclase crystals. Note white arrows indicating interconnected interstitial quartz, plagioclase with limpid rims, and resorbed plagioclase. (G) Claveix granite showing porphyritic texture with globular, corroded quartz. (H) Gelles granite in XPL, showing coarse-grained matrix texture.

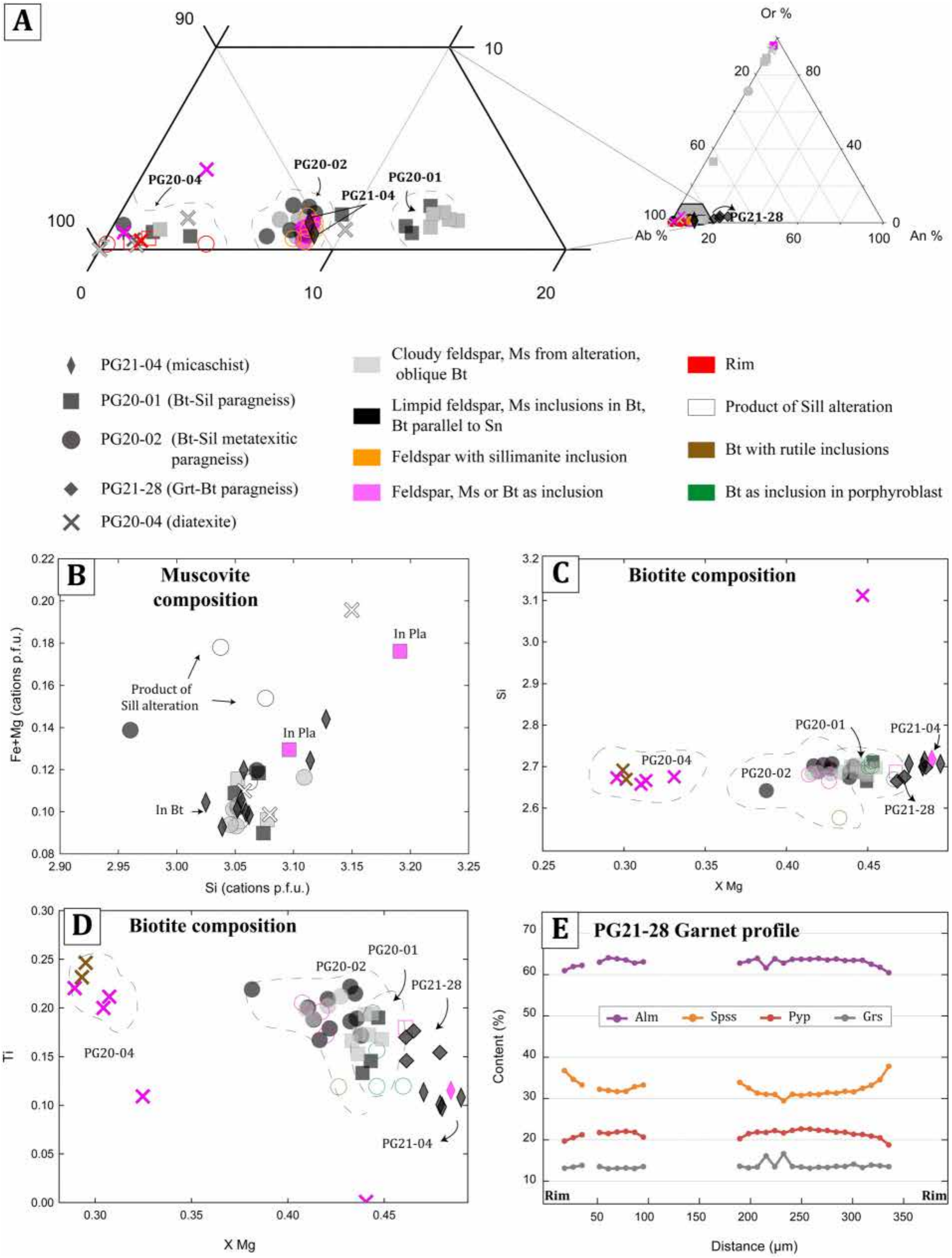

Fig. 5. Mineral chemistry results from electron microprobe analyses in micaschist (PG21-04), paragneiss (PG20-01, PG20-02, PG21-28) and diatexite (PG20-04) samples. (A) Feldspar ternary diagram. (B) Fe + Mg versus Si contents in muscovite. (C–D) Biotite Si and Ti a.p.f.u. compositions versus Mg# (100 × Mg/[Mg + Fe^{2+}]). (E) Garnet composition shown as molar proportions of end-member compositions (Alm = almandine, Grs = grossular, Prp = pyrope, Sps = spessartine) across a crystal profile.

4.5.2 U-Pb–Pb dates

Micaschist sample PG21-04 exhibits U–Pb date distribution as the two paragneiss samples, with a prominent peak of Ediacaran dates (550–650 Ma) tailing down to *ca.* 800 Ma. However, older dates are much less frequent than observed in other samples, with only 3 concordant analyses yielding dates >800 Ma. The youngest concordant zircon population in this sample provides a Concordia date of 572.5 ± 7.2 Ma (MSWD = 1.5, n = 21, Fig. 7 A–B).

Some analyses in paragneiss sample PG20-01, mostly from zircon rims, do not provide concordant U–Pb dates, due to variable amounts of common Pb and/or Pb loss (Fig. 7C). Concordant analyses (n = 91), show a large variety of U–Pb dates, ranging from *ca.* 3325 to 545 Ma with a distinguished important population at *ca.* 600 Ma (Fig. 7C, inset). In addition, the date distribution is characterised by a few analyses with Archean dates, a Paleoproterozoic population between 2300 Ma to 1800 Ma, and a gap between 1400 Ma to 1000 Ma (Fig. 14C). The youngest population of this sample provides a Concordia date of 571.8 ± 8.2 Ma (MSWD = 0.75; n = 13, Fig. 7D).

Metatexitic paragneiss PG20-02 sample shows a very similar date distribution as that from PG20-01 presented above, except for the higher proportion of concordant Archean and Paleoproterozoic dates, notably a prominent peak at *ca.* 2000 Ma (Fig. 7E). The youngest concordant zircon population in this sample provides a Concordia date of 588.9 ± 7.1 Ma (MSWD = 1.6, n = 24, Fig 7E).

Diatexite sample PG20-04 presents a very large range of zircon U–Pb dates, with a statistical distribution very close to that of PG20-01 (Fig. 7F), *i.e.,* an important population with concordant Neoproterozoic (909-543 Ma) dates, a lack of Mesoproterozoic (<1700 Ma and >1000) grains and minor populations of Paleoproterozoic (2303-1700 Ma) dates. Many analyses, especially from zircon rims, are strongly discordant presumably due to the presence of common Pb and/or Pb loss.

In the Claveix porphyritic granite sample PG20-05, there are as few concordant grains as in sample PG20-03 (Fig. 8A) but they all cluster together, defining a Concordia date of 338.0 ± 7.3 Ma (MSWD = 1.4; n = 6) (Fig. 8B). This date is identical within uncertainty to a lower intercept date of 333.7 ± 6.8 Ma (MSWD = 1.9; n = 28) calculated by the Discordia method including most of the variably discordant analyses spreading along a mixing line between radiogenic and common Pb (Fig. 8A).

Zircons from the Gelles granite sample PG20-03 present a large proportion of discordant dates, but concordant analyses show a dominant population at *ca.* 320 Ma, together with minor Neoproterozoic and Paleoproterozoic dates (Fig. 8C). Six out of 40 analysis from the Gelles granite are concordant and yield a Concordia date of 323.3 ± 9.7 Ma (MSWD = 2.2; n = 6) (Fig. 8D). Many of the discordant analyses define a linear trend connecting these concordant points to a common Pb endmember (Fig. 8C) and thus possibly corresponding to a mixing line between radiogenic and common Pb. The lower intercept, Discordia date obtained from most analyses along this trend is 323.1 ± 5.4 Ma (MSWD = 1.6; n = 22), which is statistically undistinguishable from the Concordia date.

4.6 Lu-Hf–Hf analysis on zircon

Lu–Hf isotopic analysis of concordant zircon from all metamorphic and magmatic samples show a wide range of εHf(t) values from +13.6 to -25.5 (typical uncertainties are ± 1.5 εHf(t) units) (Fig. 9A–B). Zircons from micaschist PG21-04, paragneiss PG20-01, metatexitic paragneiss PG20-02 and diatexite PG20-04, as well as the few >500 Ma zircons from Claveix porphyritic granite PG20-05 and Gelles granite PG20-03, overlap in both age and εHf(t) values. The dominant population of zircon with Ediacaran U–Pb dates found in all samples notably spreads over the entire range of εHf(t) values, whereas the Paleoproterozoic and Archean populations show a more limited variability (*ca.* +5 to -10 with only few outliers at more positive or negative values).

For the two plutonic rocks, the initial εHf(t) values were calculated for each granite based on the dates of the main zircon populations (see section about U–Pb dating). The Claveix porphyritic granite shows on average less radiogenic zircon Hf isotopic composition than the Gelles granite, with average εHf(t) values of -5.2 ± 0.6 (2 S.D., n = 7) and -2.2 ± 1.2 (2 S.D., n = 8), respectively.

4.7 Monazite dating

4.7.1 Monazite textures

Monazites from the investigated samples range in size from 10 to 50 μm. In the paragneiss PG20-01 and metatexitic paragneiss PG20-02, monazite occurs mostly as inclusion in biotite, along its cleavage planes or as elongated crystals or clusters of crystals along the grain boundaries of minerals defining the main foliation (Fig. 10 A–B). Monazite is also present in sillimanite aggregates. In the diatexite sample PG20-04, monazite occurs as inclusion in feldspar or quartz of the granitic matrix, or within the metatexites enclaves associated with biotite and sillimanite,*i.e.,* the mesosome (Fig. 10C). Chemical maps reveal that monazite grains from all samples do not usually exhibit internal zonation, although some rare grains show a core enriched in Th related to rims.

4.7.2 Monazite Dates

Monazite U–Pb data from all samples show a simple distribution characterised by a dominant, if not exclusive population of concordant Carboniferous dates (Fig. 11). For all samples, it is possible to calculate Concordia dates using a majority of the data points, respectively 347.2 ± 3.8 Ma (MSWD = 1.3; n = 20) and 342.2 ± 4.6 Ma (MSWD = 1.4; n = 15) for two different thin sections of paragneiss sample PG20-01; 347.1 ± 4.2 Ma (MSWD = 0.38; n = 48) for metatexitic paragneiss sample PG20-02; and 357.6 ± 1.5 Ma (MSWD = 1.5; n = 30) for the diatexite PG20-04. There is no clear correlation between U–Pb age and textural location. Within a given sample, monazite grains from different textural positions, or different chemical domains within single grains (*e.g.* Th-rich core *vs.* Th-poor rim), most commonly show overlapping U–Pb dates. Conversely, some monazites showing significantly older dates (.*ei.* >360 Ma), or on the contrary,

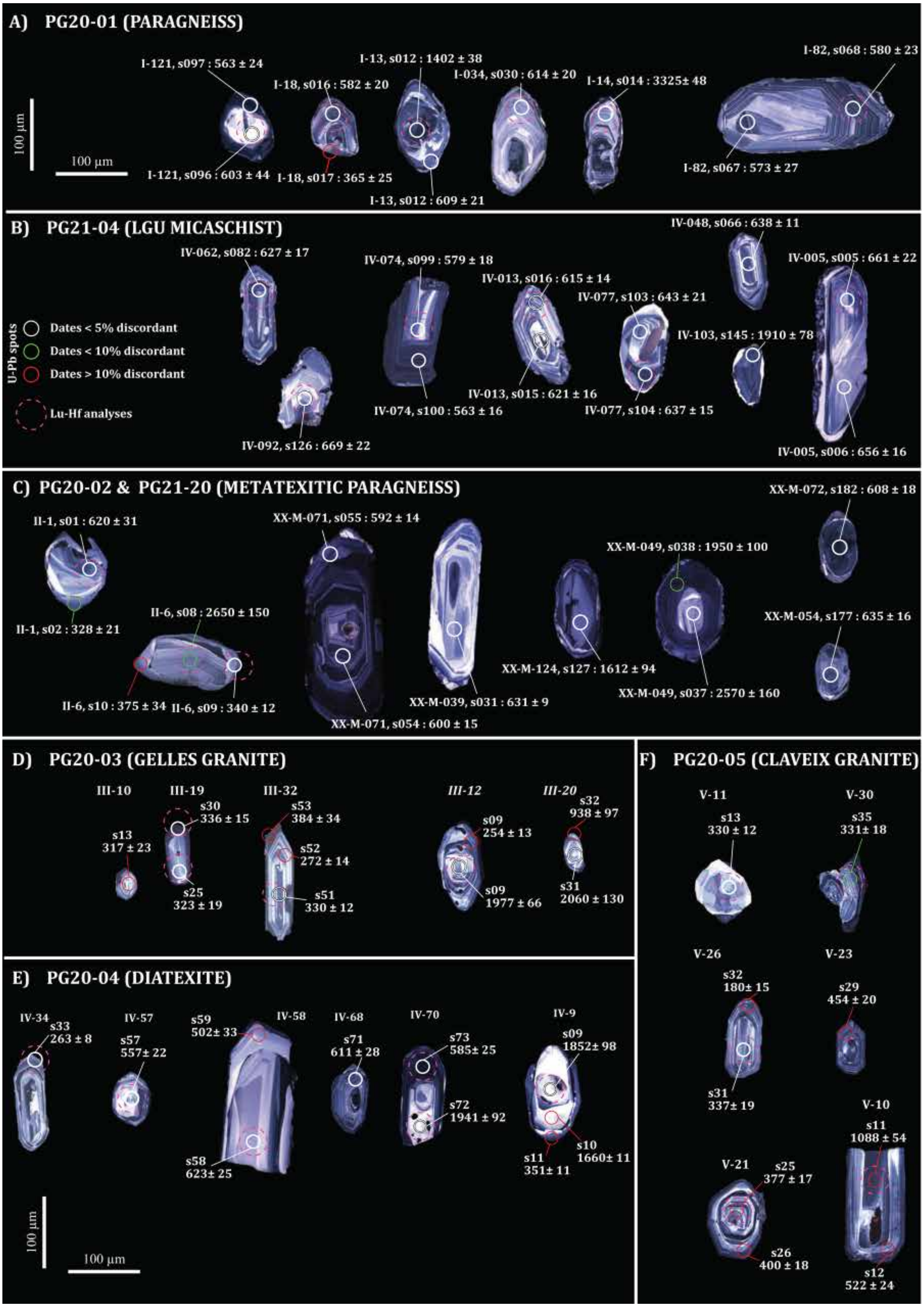

Fig. 6. Representative cathodoluminescence images of zircons from (A) PG20-01 paragneiss; (B) PG21-04 micaschist; (C) PG20-02 paragneiss; (D) PG20-03 Gelles granite; (E) PG20-04 diatexite; and (F) PG20-05 Claveix granite.

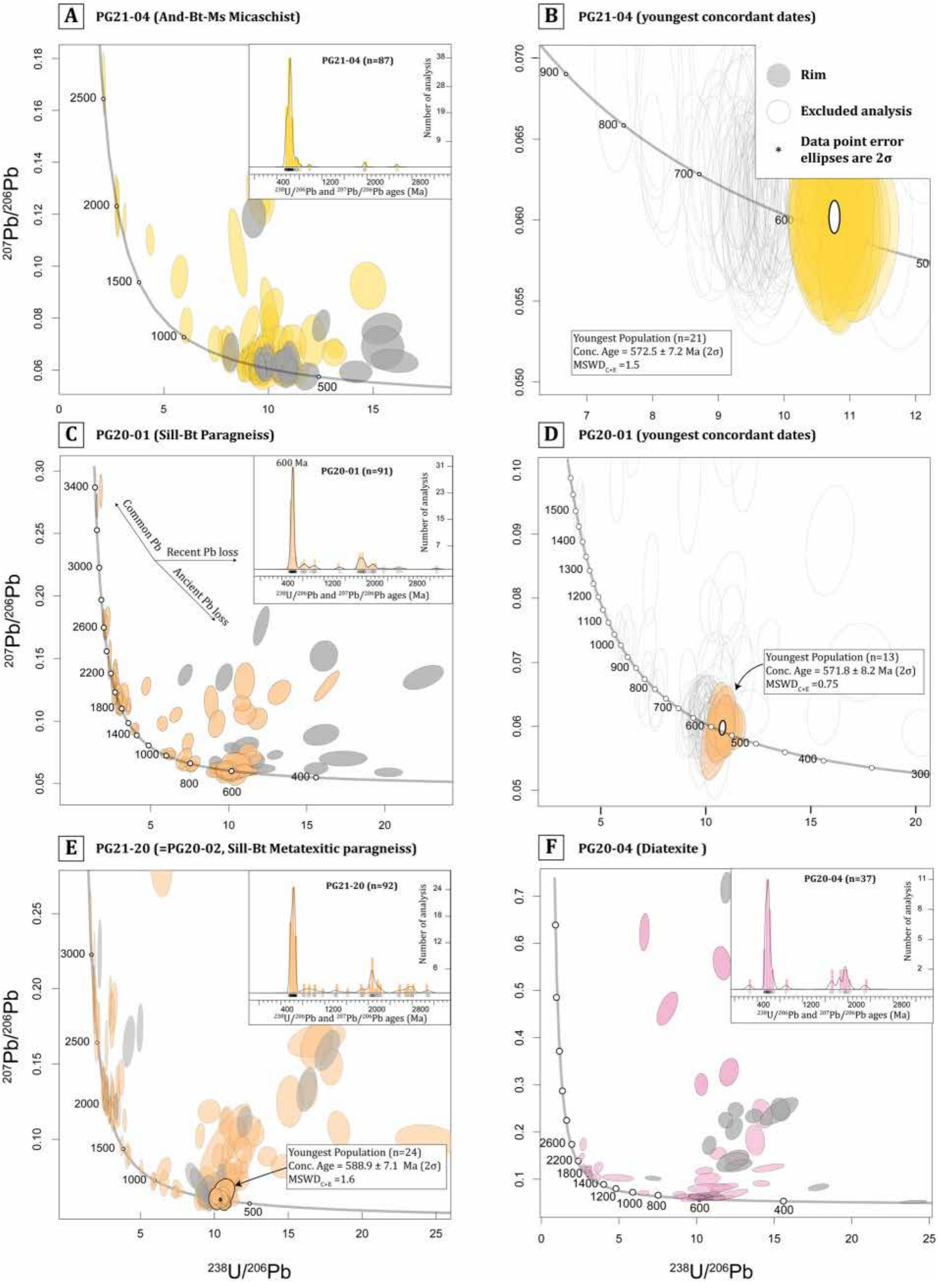

Fig. 7. Concordia diagrams (Tera–Wasserburg, ^{238}U/^{206}Pb *vs.* ^{207}Pb/^{206}Pb) and kernel density estimate (KDE) plots showing the distribution of U–Pb isotopic analyses for metasedimentary rocks: (A–B) PG21-04 micaschist; (C–D) PG20-01 paragneiss; (E) PG20-02 paragneiss; and (F) PG20-04 diatexite. In (A), (C), (E) and (F), grey circles indicate rim analyses; in (B) and (D), empty circles are excluded from the calculation of Concordia dates. Only analyses with less than 5 per cent discordance (^{206}Pb/^{238}U ÷ ^{206}Pb/^{207}Pb age × 100) are included in the KDE plots.

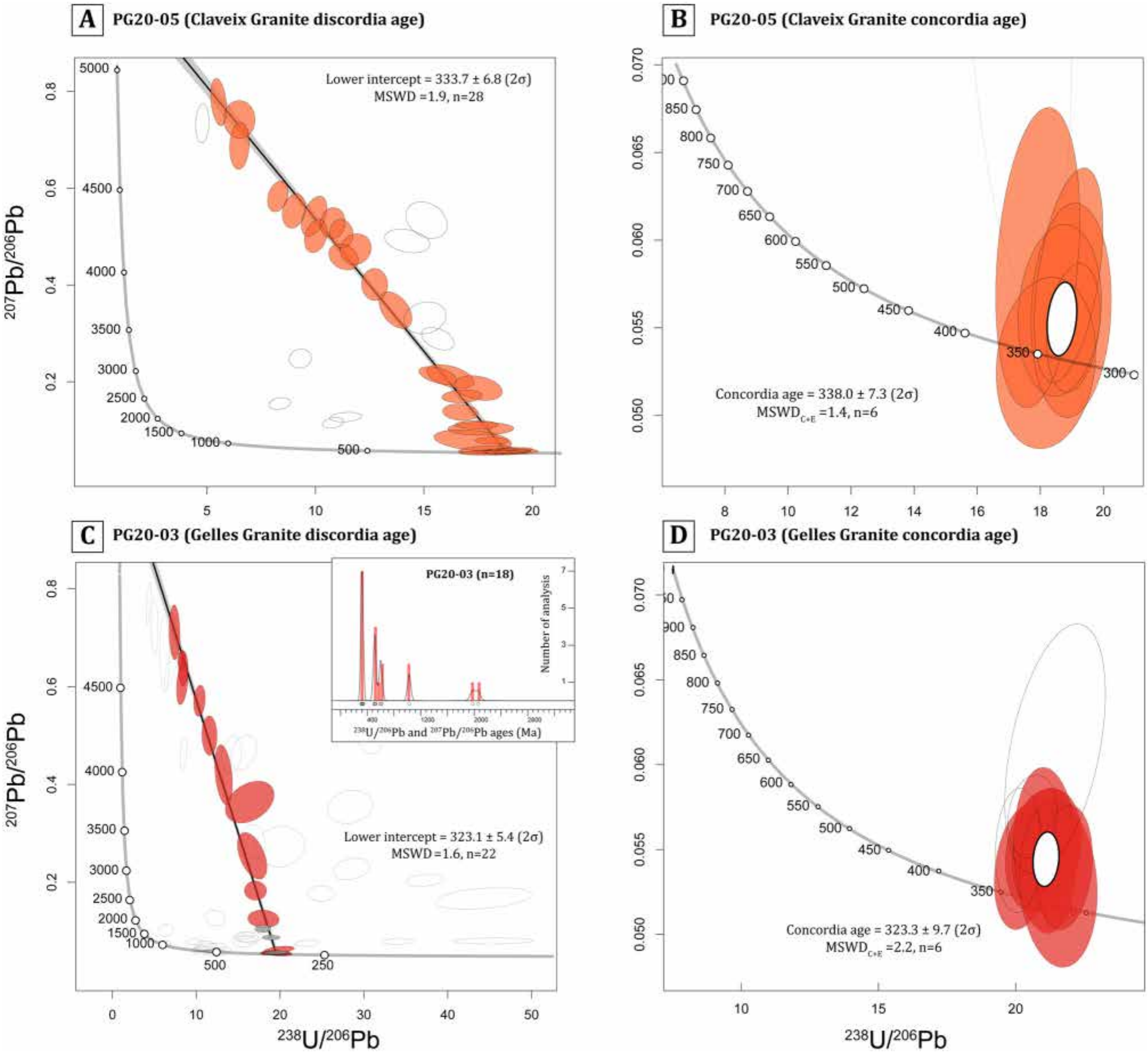

Fig. 8. Concordia Tera–Wasserburg diagrams and KDE plots showing the distribution of U–Pb isotopic analyses for plutonic rocks: (A-B) Claveix-related porphyritic granite; (C-D) Gelles granite. Empty circles are excluded from the calculation of Concordia and Discordia dates; grey circles indicate rim analyses.

younger dates as in the case of the diatexite in which a few concordant analyses (n = 4) decreased to *ca.* 300 Ma, do not seem to be associated to a peculiar textural position as they are present both in leucosome and as inclusions in biotite.

On the other hand, in a few cases, distinct U–Pb dates were obtained from different spots within single crystals of monazite, pointing to a zonation that is not identified from BSE images or X-ray maps.

4.8 Discussion

4.8.1 A metamorphic gradient from micaschists-paragneiss to diatexites

Our field investigations confirm the structural and metamorphic trends of the studied area near Pontgibaud, as originally proposed (Tempier, 1969; Tempier, 1974; Fernandez and Tempier, 1977). Namely, micaschsits and paragneiss exposed to the south of the studied display a shallow–Dipping dominant foliation that is transposed in a steep–Dipping foliation toward the Sillon Houiller to the West and into a step–Dipping synmigmatitic foliation of the migmatitic paragneiss. This transposition is consistent with a metamorphic gradient delineated by metamorphic isograds mapped by Tempier (1967). We further document this metamorphic gradient with-P–Testimates obtained from pseudosection calculations.

The main mineral assemblage of sample micaschist PG21-04 is plagioclase + muscovite + biotite + quartz with rare andalusite and altered porphyroblast interpreted as pseudomorphs after cordierite (Fig. 4A and B). This assemblage is stable in a restricted-P–Tfield at 2.3 ± 0.3 kbar

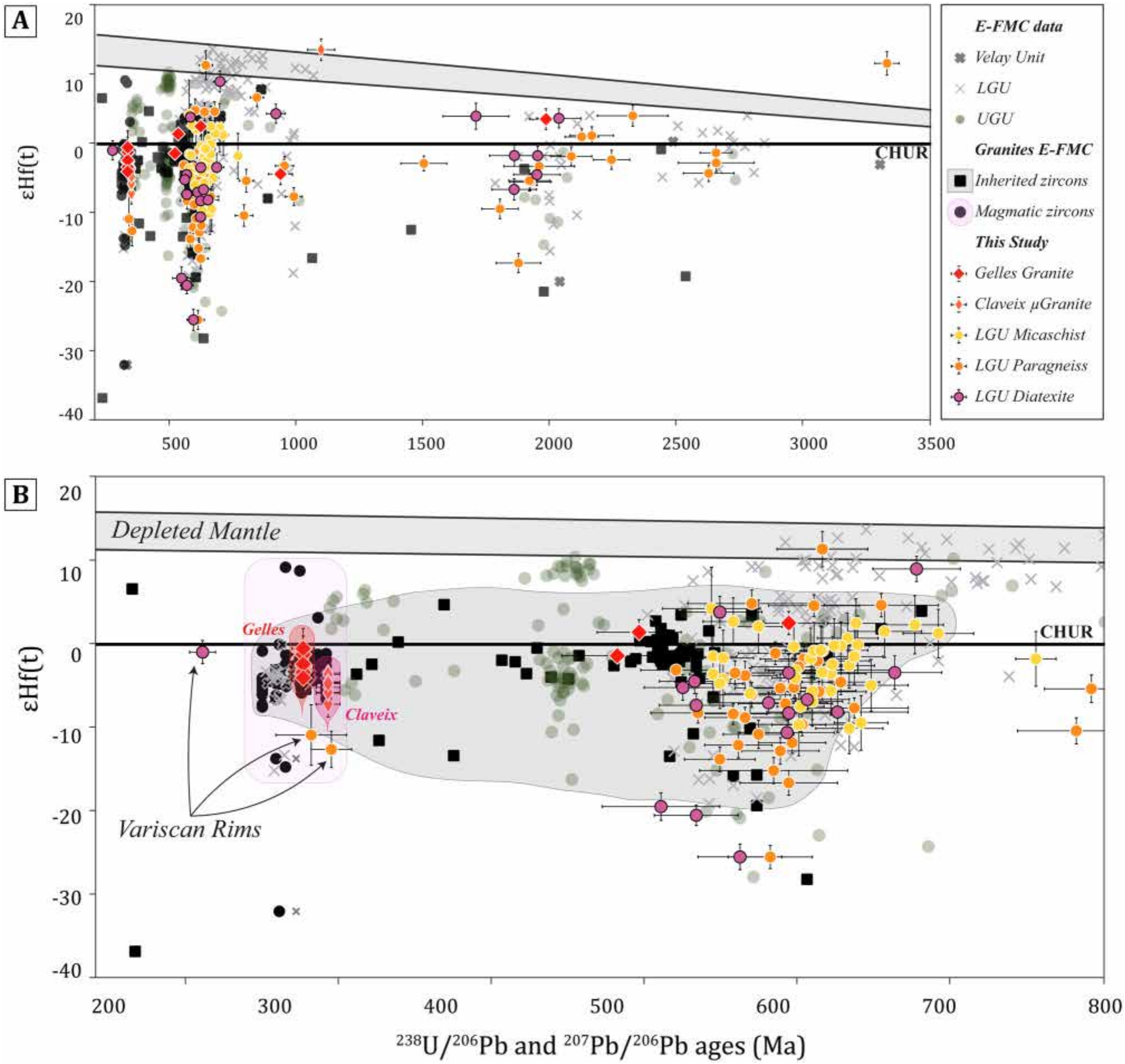

Fig. 9. Zircon Lu–Hf compositions for samples from this study and from the eastern French Massif Central (FMC) literature, expressed as εHf(t) versus U–Pb age, with (a) zircon ages from 200 Ma to 3500 Ma; and (b) zircon ages from 200 Ma to 800 Ma. Grey and pink areas represent inherited cores and magmatic zircons from S-type granites (Moyen *et al.*, 2017), respectively. Zircon data for the Velay unit, LGU and UGU are compiled from (Chelle-Michou *et al.*, 2017; Couzinié *et al.*, 2019).

and 570 ± 20 °C, within the stability field of rutile that occur in the matrix of the sample. Ilmenite may have formed at higher temperature conditions at *ca.* 650 °C. With decreasing temperature from the Bt Fsp Crd San Qz Ilm field, K–Feldspar and cordierite modes decrease while muscovite, plagioclase and biotite modes increase in proportion reaching relatively equal amounts of 10-15 per cent in the lower temperature stability field containing andalusite and rutile, consistent with thin section observations.

Paragneiss sample PG20-01 contains biotite + plagioclase + K–Feldspar + quartz + sillimanite and cordierite replaced by sericite. Concordant leucosome is observed in macroscopic specimen. Muscovite as inclusion in biotite and feldspar suggests that it corresponds to a relic from a lower grade paragenesis. The mineral assemblages correspond to a restricted-P–Tfield around 3 ± 1 kbar and 650 ± 20 °C. In this field 10-20 per cent liquid is produced, and biotite composition is consistent with those observed in thin section (X_{Fe} *ca.* 55, Ti = 0.13-0.19 a.p.f.u). Sillimanite replacement by muscovite suggests a path with decreasing temperature, where muscovite increases abruptly from this field while sillimanite decreases, and the anorthite content of plagioclase

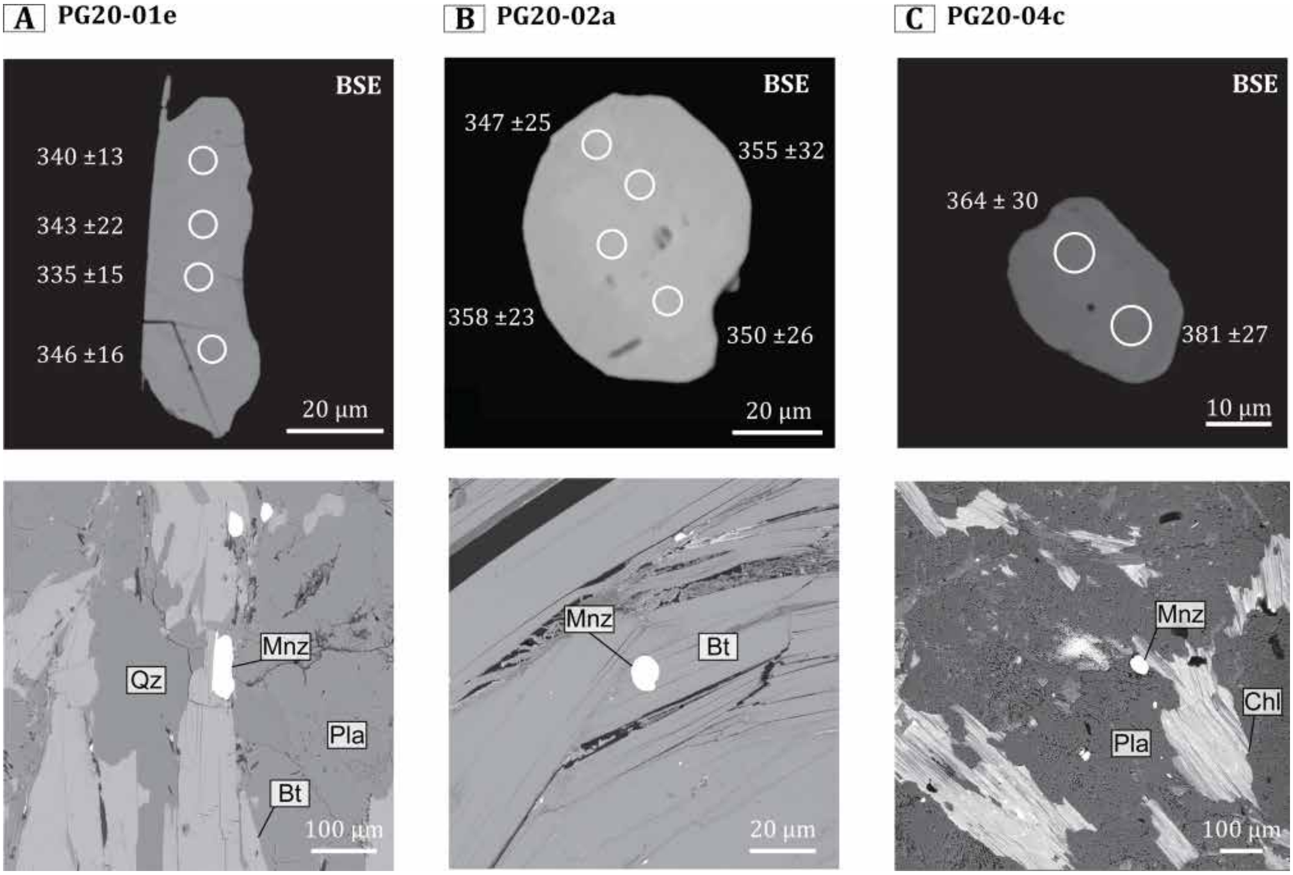

Fig. 10. Representative backscattered electron images of metamorphic monazites from paragneiss PG20-01 and PG20-02, and diatexite PG20-04, with corresponding lower-magnification and higher-brightness images showing the textural context of the grains. White circles indicate the location of analysis spots and corresponding individual ^{206}Pb/^{238}U dates.

composition decreases down to 15 per cent X_{An}. This trajectory probably extended to the biotite + plagioclase+ cordierite + muscovite + quartz field at *ca.* 2.6 kbar and *ca.* 530 °C (Fig.12C–D).

The dominant mineral paragenesis of paragneiss sample PG21-28, sillimanite + garnet + biotite + plagioclase with rare rutile inclusions in garnet and biotite-sillimanite intergrowth, is stable in a restricted-P–T field between 660 °C ± 10 °C and 5.3 ± 1.0 kbar (Fig.13A-B). Compositional zoning in garnet indicates a decreasing temperature towards the Bt+Fsp+Grt +Ilm+Ms+Qz field at lower temperature, consistent with minor late muscovite and rare ilmenite observed in the matrix. From this field, sillimanite, garnet, biotite and plagioclase modes increase with decreasing muscovite. The Mn enrichment observed in garnets' compositional profiles (Fig. 5E), along with isopleths calculated for this sample, collectively suggest reequilibration at lower temperature compared to the core. The -Core–rim zonation zonation is consistent with a retrogressive path implying a temperature decrease of about 70°C. Leucosome is not recognised neither at microscopic nor macroscopic scale but thermodynamic modelling indicates an increase in melt up to 10 vol. per cent with increasing temperature within the inferred stability field. This suggests that some melt might have escaped this rock.

Metatexitic paragneiss sample PG20-02 contains biotite + plagioclase + quartz + sillimanite as well as porphyroblasts interpreted as cordierite pseudmorphs replaced by sillimanite-rich assemblages. Minute garnet is locally observed but could not be analysed due to its small size (< 200 µm) and the presence of numerous graphitic inclusions. Isolated leucosomes (max 10 vol. per cent) were also observed at the macroscopic scale. The mineral assemblages correspond to a restricted-P–Tfield around 5 ± 1 kbar and 650 ± 50 °C. The composition of biotite (X_{Fe} = 55–58 and Ti = 0.15–0.19 a.p.f.u.) indicates maximum temperatures around 675°C just above 5 kbar (Fig.13C-D). Note that large biotite crystals included into cordierite pseudomorphs have systematically low X_{Fe} values (*ca.* 55) compatible with growth of cordierite at pressure between 5 and 6 kbar. Garnet is predicted at these conditions but in very low proportions (~1 vol per cent), in agreement with petrographic observations. Retrogression of large cordierite porphyrolasts into sillimanite-rich assemblages suggests decreasing temperature between 675 and 650°C where the proportion of cordierite decreases and the one of sillimanite increases. The complete retrogression of cordierite porphyroclasts is consistent with a retrograde path extending toward the cordierite-out line located near 600°C between 5 and 4 kbar. The presence of plagioclase grains with sillimanite inclusions is also consistent with such a retrograde path, along which plagioclase content increases steadily (from 20 vol. per cent around 675 °C to 40 vol. per cent at 650 °C near 5 kbar) while sillimanite mode only increases moderately. Accordingly, plagioclase An content

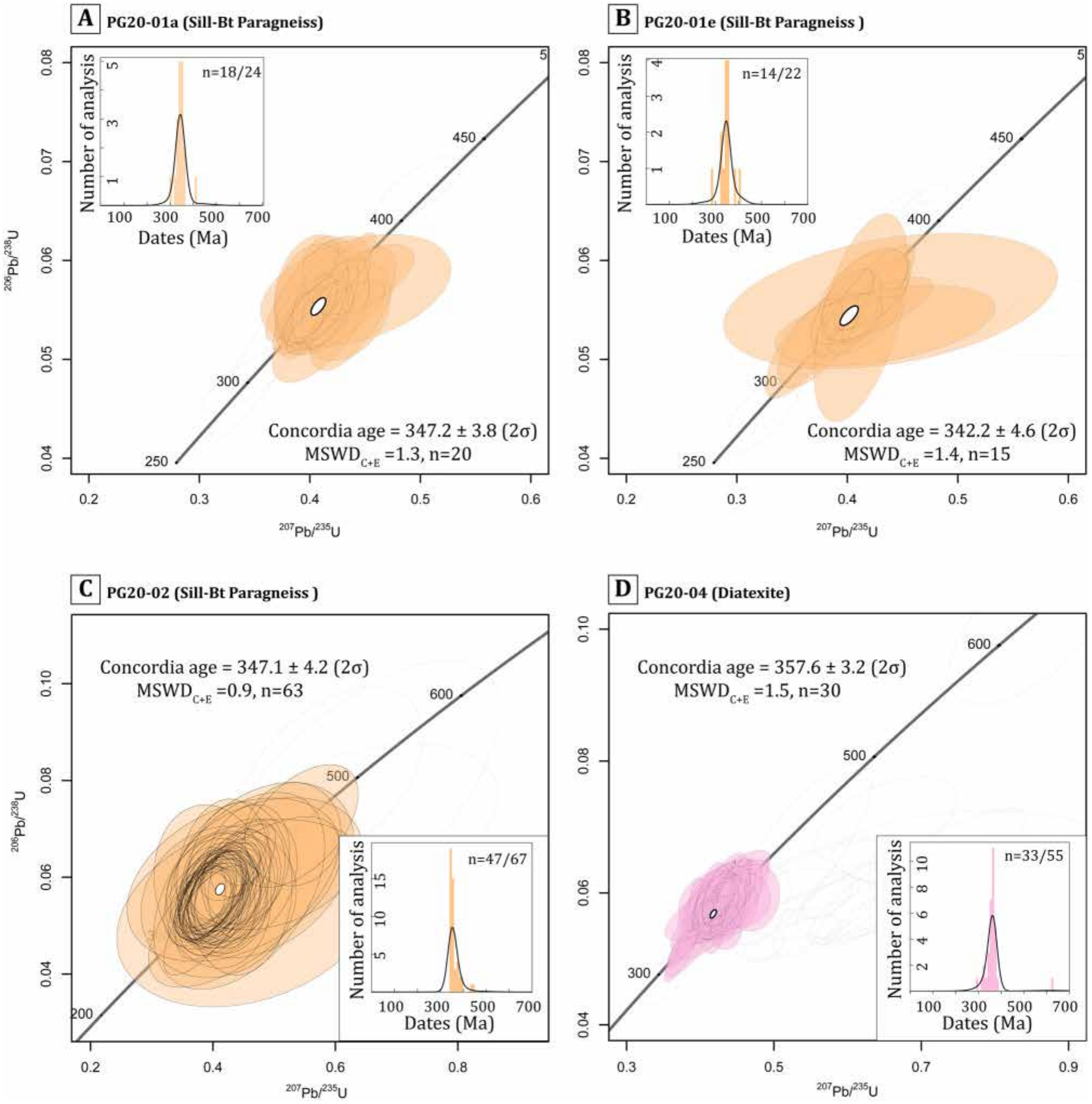

Fig. 11. Concordia Tera–Wasserburg diagrams and KDE plots for monazites from paragneiss (a–b) PG20-01, (c) PG20-02, and diatexite (d) PG20-04. Empty circles represent analyses excluded from the calculation of Concordia dates.

is compatible with temperatures below 650 °C. Collectively, the textural record, mineral modes and compositions thus indicate a retrograde path starting around 675 °C and 5.5 kbar down to 600 °C and 4.5 kbar.

These data are consistent with a continuous, high-temperature//low-pressure metamorphic gradient from micaschists-paragneiss to migmatites with a pressure that ranges from *ca.* 2 to 5 kbar and temperature increasing from *ca.* 570 to 660 °C from South to North. We propose that this metamorphic gradient is representative of the thermal state of the Variscan orogenic crust after the climax of crustal thickening and following significant thermal relaxation.

4.8.2 Interpretation of zircon/monazite data

The youngest population of zircons in micaschist PG21-04, paragneiss PG20-01, and metatexitic paragneiss PG20-02 provides Concordia dates of 572.5 ± 7.2 Ma (MSWD = 1.5, n = 21, Fig. 6F), 571.8 ± 8.2 Ma (MSWD = 0.75; n = 13, Fig. 7B) and 588.9 ± 7.1 Ma (MSWD = 1.6, n = 24, Fig. 6C), respectively. Considering the metasedimentary nature of these samples and the likely detrital nature of the zircon population with strongly variable U–Pb dates, these dates are interpreted as reflecting the maximum deposition age of the sedimentary protoliths. Zircons from diatexite sample PG20-04 do not provide any reliable age

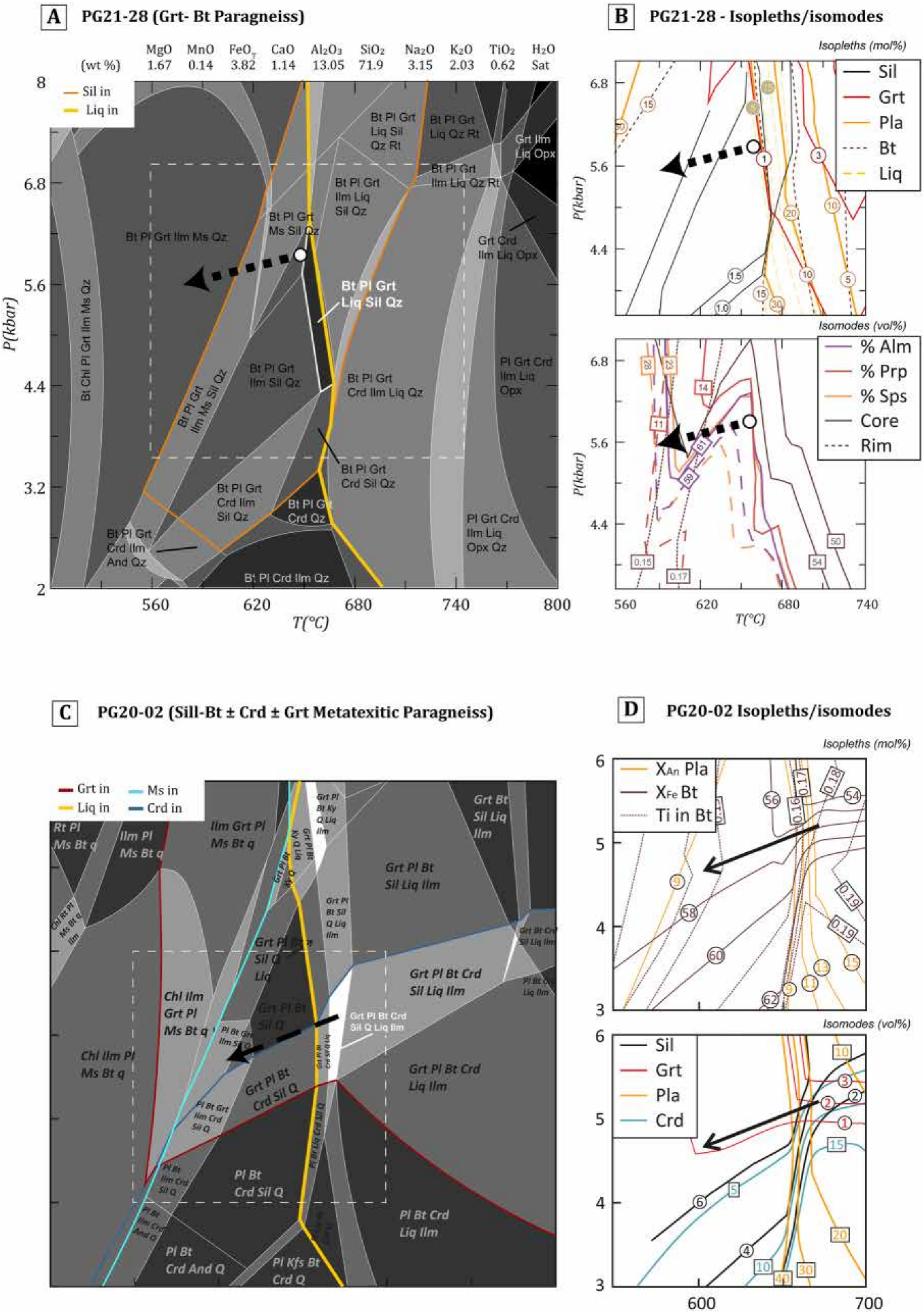

Fig. 12. Results of thermodynamic modelling shown as P–T pseudosections (a, c) and isopleth and isomode contours (b, d) for micaschist PG21-04 (a–b) and paragneiss PG20-01 (c–d). Bulk compositions (in oxide wt. per cent) used for calculations are indicated. Coloured lines represent the appearance of index minerals. Arrows indicate P–T paths from peak to retrograde conditions.

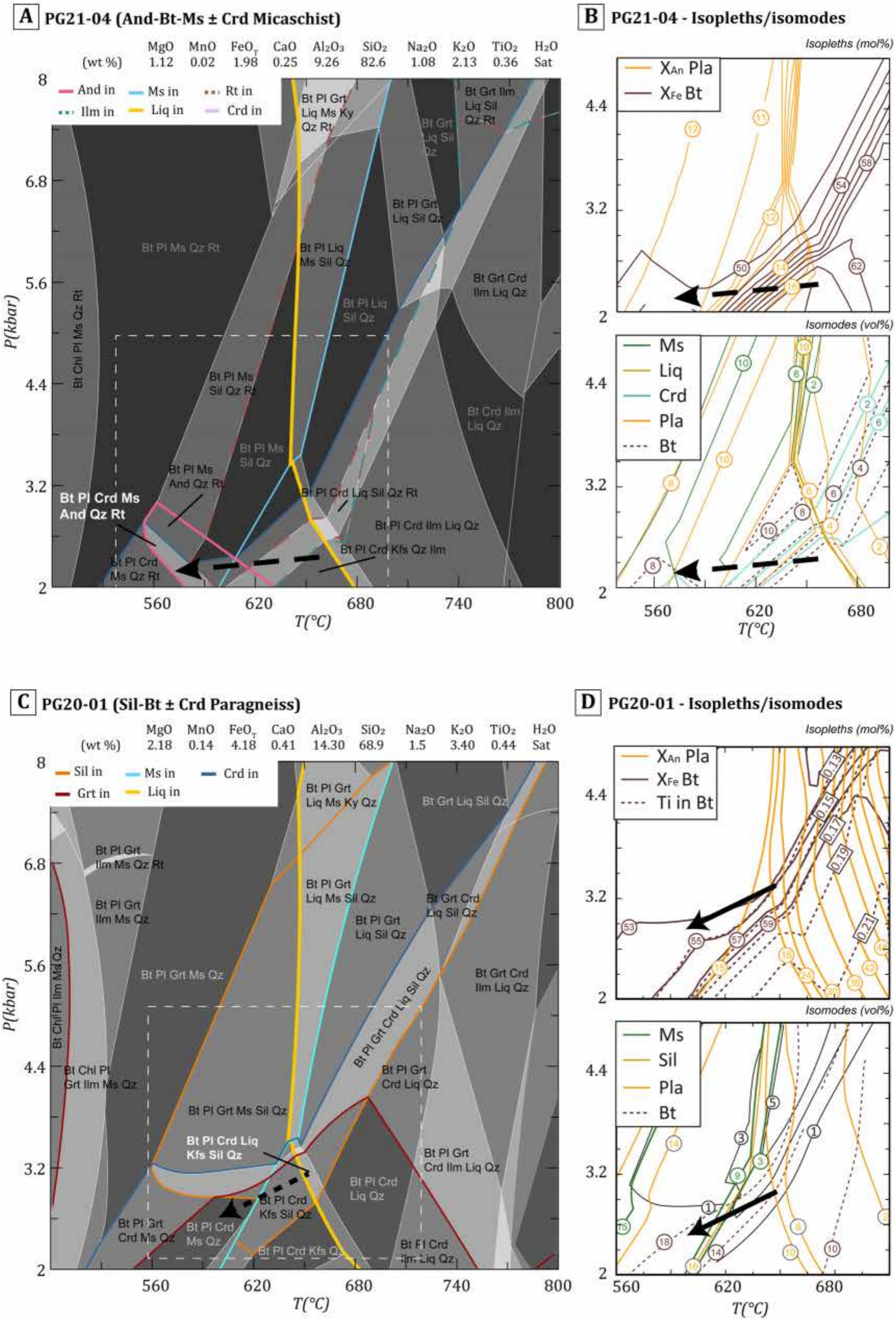

Fig. 13. Results of thermodynamic modelling shown as P–T pseudosections (A, C) and isopleth and isomode contours (B, D): (A–B) for paragneiss PG21-28, and (C–D) for paragneiss PG20-02. Bulk compositions (in oxide wt. per cent) used for calculations are indicated. Coloured lines represent the appearance of index minerals. Arrows indicate P–T paths from peak to retrograde conditions.

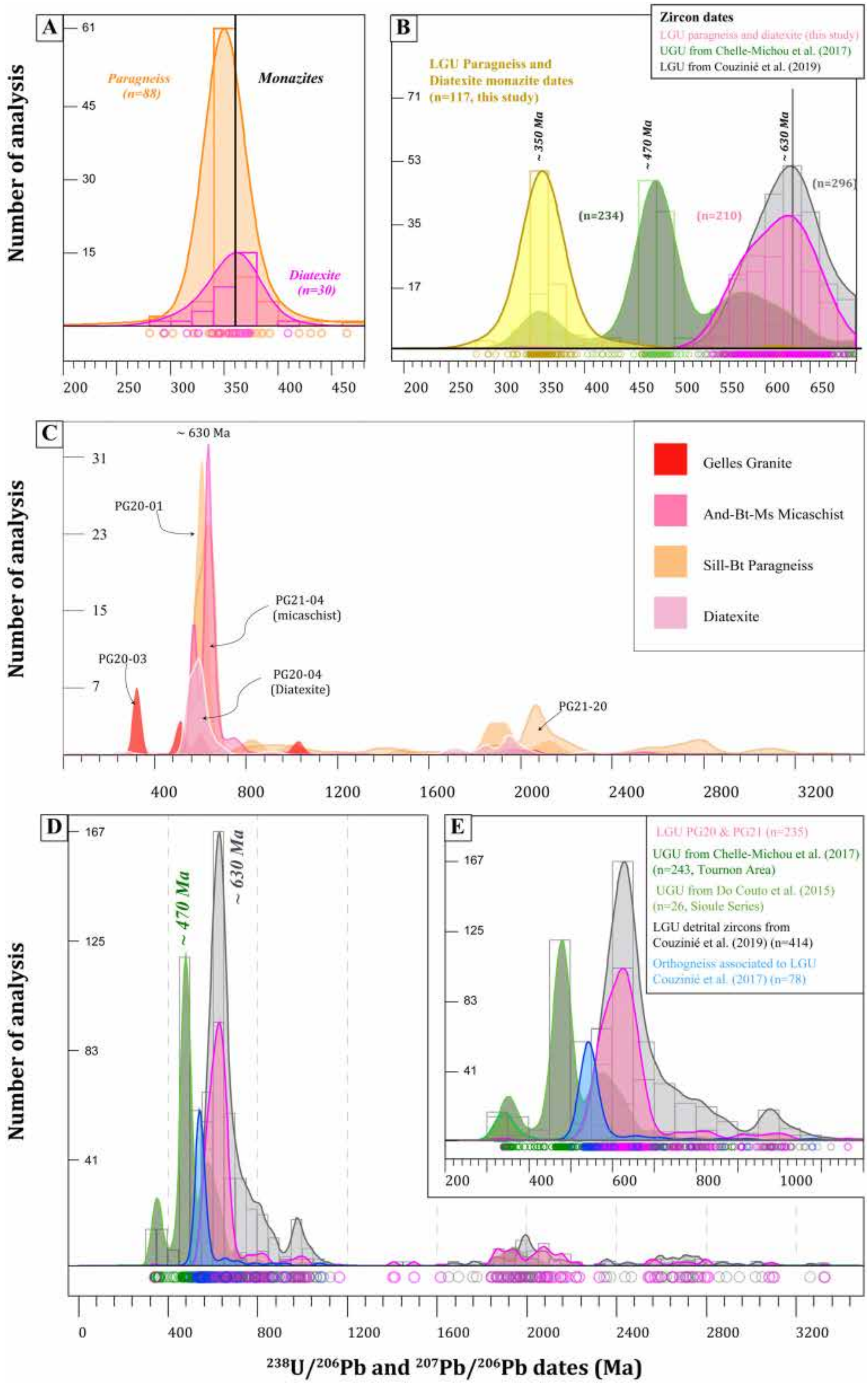

Fig. 14. KDE plots of U–Pb dates (^{206}Pb/^{238}U for dates younger than 1200 Ma; ^{206}Pb/^{207}Pb for dates older than 1200 Ma), comparing zircon and monazite data from this study with published data from the eastern French Massif Central (FMC). (A) Monazite ^{206}Pb/^{238}U dates' distribution for paragneiss and diatexite (this study). (B) Monazite and zircon ^{206}Pb/^{238}U dates for LGU paragneiss (this study) and zircon dates for LGU and UGU (from Chelle-Michou *et al.*, 2017; Couzinié *et al.*, 2019). (C–D) Distribution of zircon dates of metasedimentary rocks from this study and from LGU, UGU and orthogneiss in the eastern FMC (compiled from Chelle-Michou *et al.*, 2017; Couzinié *et al.*, 2017, 2019; Do Couto *et al.*, 2016).

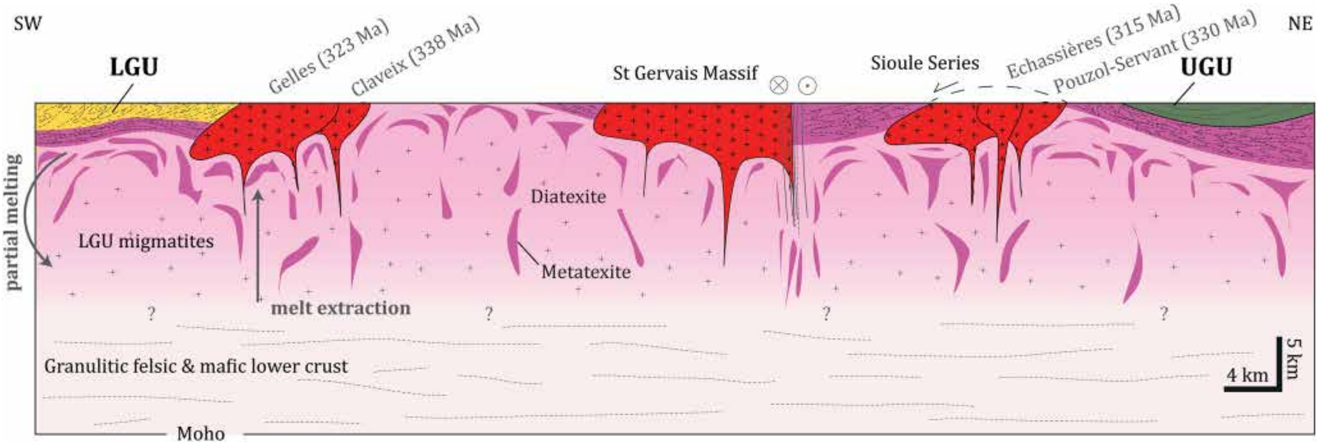

Fig. 15. Model for the Variscan crustal structure in the Pontgibaud region. LGU paragneiss and migmatites are exposed from Pontgibaud to the St Gervais Massif northwards. The transition from paragneiss to metatexite and diatexite is gradual. At depth, migmatites are products of partial melting of LGU and are abundant down to the granulitic lower crust. In this model, granites, migmatites and paragneiss are genetically linked.

that would correspond to Variscan metamorphism. The range of U–Pb dates is therefore interpreted as reflecting mainly inherited zircon from - meta–sedimentary protoliths, similar to the micaschist and paragneiss.

The Concordia dates of 338.0 ± 7.3 Ma and 323.3 ± 9.7 Ma obtained on euhedral, oscillatory-zoned magmatic zircon of the Claveix porphyritic granite (PG20-05) and the Gelles granite (PG20-03), are interpreted to represent the ages of crystallization of these plutons. In previous work, the Claveix granite was already identified to be older than the Gelles granite (Fernandez, 1969; Négroni, 1981; Hottin *et al.*, 1989) and was argued to be synchronous with the emplacement of Upper Visean volcanic tuff at *ca.* 335–330 Ma (Hottin *et al.*, 1989). This magmatic event at 340–330 Ma has been documented throughout the northeastern FMC (Binon and Pin, 1989; Laurent *et al.*, 2017). In turn, the crystallisation age of the Gelles pluton is consistent with the previously published Rb–Sr mineral isochron age of 319 ± 12 Ma (Fernandez, 1969).

Monazite grains in paragneiss samples, which show a dominant population of concordant dates, are unzoned, embedded in the minerals of the main paragenesis of the rock (biotite, sillimanite, and quartzo–feldspathic leucosome) and are and aligned with the main foliation of the rock. Accordingly, monazite likely crystallised in the-P–Tconditions inferred for the main paragenesis of the samples and monazite U–Pb Concordia dates ranging from 357.6 ± 1.5 Ma to 342.2 ± 4.6 Ma are interpreted as dating the corresponding metamorphic event. The small number of concordant ages older than *ca.* 360 Ma were all obtained on crystals included in high-temperature minerals (biotite, sillimanite) or assemblages (leucosome), thus possibly corresponding to the age of the onset or prograde stage of the HT event.

In diatexite PG20-04, monazite dates as old as 600 Ma are interpreted as inherited, which suggests that the temperature of partial melting was not high enough to insure complete dissolution-resetting of pre–Existing monazite and zircon grains (Rubatto *et al.*, 2001; Kelsey *et al.*, 2008; Yakymchuk and Brown, 2014; Guergouz *et al.*, 2018). This is consistent with the lack of metamorphic rims in zircons from micaschist, paragneiss, metatexite and diatexite samples. This feature was recognised in other migmatites of the FMC corresponding to low-temperature melting (Couzinié *et al.*, 2021) and, predicted from thermodynamic modelling, which shows that at <700 °C, a maximum 10 per cent zircon and 40 per cent monazite from the rock can be dissolved in the melt phase (Kelsey *et al.*, 2008).

On the other hand, the presence of a few (n = 4) concordant monazite analyses showing U–Pb dates younger than 357.6 ± 1.5 Ma in this sample could be interpreted as recording protracted monazite crystallization throughout metamorphism and subsequent melting. Alternatively, given the diatexite nature of PG20-04, monazites with a range of ages could be incorporated through mechanical mixture of fragments of rocks and melts from different protoliths, coming from a deeper crustal level and possibly recording different metamorphic ages. However, none of these two hypotheses is consistent with the fact that diatexite PG20-04 is cross–Cut with sharp contacts by Claveix porphyritic granite (sample PG20-05) that crystallised at *ca.* 338 Ma (see above), indicating that the migmatites had already cooled down and were significantly exhumed at this time. Therefore, this range of monazite ages likely rather reflects late disturbance of the U–Pb system, presumably due to the intrusion and/or late magmatic hydrothermal activity related to the Claveix and Gelles granite.

4.8.3 Links between metamorphic and magmatic units in the Pontgibaud area

As presented in the previous sections, the compositions, assemblages, metamorphic evolution and ages of micaschists-paragneiss, migmatites and granites in the Pontgibaud area support that these rocks are genetically linked. The gradual field transition from micaschists to migmatites and the corresponding, continuous Low-Pressure/High-Temperature metamorphic gradient further suggest that these rocks are part of the same lithotectonic unit showing different exposure levels (shallower in the South, deeper in the North). From this perspective, and the steep–Dipping synmigmatitic foliation of the migmatites would correspond to the transposition of the shallow–Dipping foliation of the metasedimentary rocks.

U–Pb dating of metamorphic monazite points to broadly synchronous amphibolite–Facies metamorphism in all samples (Fig. 14A–B) at *ca.* 355-345 Ma. Lastly, the paragneiss and diatexite samples display a similar population of former detrital zircon ages, which is consistent with a petrogenetic link between these rocks (Fig. 14C–D), *i.e.,* a prominent peak at ~630 Ma, a lack of Stenian ages (1000-1200 Ma) and the existence of a Paleoproterozoic population of mainly Orosirian age (1800 to 2050 Ma). Former detrital zircon from the paragneiss samples and diatexite fully overlap in the Hf isotopic *vs.* U–Pb age space (Fig. 9), supporting that these rocks likely present a genetic link, *i.e.* represent a single litho-tectonic unit affected by a metamorphism that increased from South to North.

The Claveix and Gelles granites of the Pontgibaud area are peraluminous. They contain biotite, cordierite, muscovite and tourmaline, and thus correspond to Cordierite- and Muscovite Peraluminous Granites (CPG and MPG) in the classification of Barbarin (1999). Magmas of CPG/MPG compositions are common in the eastern FMC and were proposed to result from melting of the country rocks, dominantly of meta–sedimentary composition (Laurent *et al.*, 2017; Moyen *et al.*, 2017; Villaros *et al.*, 2018). Inherited zircons from the plutonic rocks present the same U–Pb age distributions (Fig. 14) and Lu–Hf isotopic characteristics (Fig. 9) as those of the paragneiss and diatexite rocks, which support the hypothesis that granites of the Pontgibaud area are potentially sourced from magma extraction derived from partial melting of meta–sedimentary rocks similar to the exposed ones, but at a deeper level of exposure (see next section for detailed discussion about this point).

Our results and interpretations have implications for the attribution of metamorphic rocks of the Pontgibaud area to the litho-tectonic units defined at the scale of the FMC. As introduced earlier (see Fig. 1 and Geological Setting), the northern vs. southern parts of the study area were respectively attributed to the UGU and LGU, with disputed location of the boundary zone depending on the authors and maps (Hottin *et al.*, 1989; Chantraine *et al.*, 2003). In any case, the superposition of the UGU over the LGU should be marked by a mylonitic contact and an inverted metamorphic gradient, which were not identified in the field. In contrast, as discussed here, all lines of evidence are rather consistent with all metamorphic rocks belonging to the same litho-tectonic unit affected by synchronous LP-HT metamorphism. The metamorphic conditions and LP-HT gradient are typical of the LGU in the region (Schulz, 2009) and in the E–FMC in general (Vanderhaeghe *et al.*, 2020), in contrast with the HP-LT gradient recorded by UGU rocks. The age of the LP-HT event of *ca.* 357-345 Ma is consistent with metamorphic ages from the LGU elsewhere in the E–FMC, notably from the nearby Sioule series (Schulz 2009; Do Couto *et al.*, 2016; Monnier *et al.*, 2021) where UGU monazites are generally younger (340–320 Ma; Schulz, 2009) and in LGU diatexites in a similar structural position in the Livradois area (Gardien *et al.*, 2011). Moreover, the range of maximum deposition ages of sedimentary protoliths in the Pontgibaud area (571.8 ± 8.2 Ma to 588.9 ± 7.1 Ma) well overlaps that of meta–sedimentary rocks of the LGU (556.8 ± 5.1 Ma to 592.4 ± 5.5 Ma) as determined by Couzinié *et al.*, (2019) in the Velay area. Finally, although zircon populations of metamorphic rocks in the Pontgibaud region show similar ages and Lu–Hf isotopic composition as those (Chelle-Michou *et al.*, 2017; Couzinié *et al.*, 2019) from both LGU and UGU samples (Fig. 9, 14), they strikingly lack the 480 Ma age peak that is typical for the UGU gneisses (Chelle-Michou *et al.*, 2017). Based on these features, we attribute the metasedimentary rocks and migmatites exposed in the Pontgibaud area to the Lower Gneiss Unit.

4.8.4 Implications for the crustal structure and geotherm

As discussed in the previous section, the Variscan metamorphic rocks of the Pontgibaud area likely belong to the LGU, in contrast with what had been proposed in previous works (Hottin *et al.*, 1989; Chantraine *et al.*, 2003). On a larger scale, the LGU rocks that outcrop with a main subhorizontal foliation in the Pontgibaud region may continue in depth northward and southward to the Sioule series and the Artense dome respectively, where the LGU is overlain by the UGU unit in km-scale folded structures (Fig. 15). Therefore, correlation of the tectono-metamorphic pattern described in this study with the data presented by Do Couto *et al.*, (2016) and Brousse *et al.*, (1990) allows the construction of a crustal model, where the plutonic units would be sourced in LGU migmatite as result of melt segregation, and the latter would represent an important proportion of the crust in depth, derived from partial melting of rocks similar to the metamorphic ones exposed at the surface (Fig. 15). Arguments supporting this interpretation are developed in the following.

Formation and extraction of large volumes of Crd-Bt granitic to granodioritic magmas such as those represented by the Claveix and Gelles plutons requires melting conditions of >800 °C, as indicated by phase equilibria modelling (Villaros *et al.*, 2018) on other E–FMC granitoids. Moreover, experimental data of partial melting of E–FMC metasediments indicate that magmas compositionally similar to the Claveix and Gelles granites are typically reproduced by melting at *ca.* 850–875 °C and 5–10 kbar (Montel and Vielzeuf, 1997). Such a temperature was not reached by the exposed metamorphic rocks. Although some of the exposed migmatites are diatexites, they still contain abundant biotite pointing to temperatures <800 °C, such that they either may not all be "*n situi*" migmatites and represent local accumulation of melts transferred from lower crustal levels; and/or were formed by water–fluxed melting induced by the emplacement and crystallization of magmas sourced in the lower crust (as proposed in the Velay dome area; Barbey *et al.*, 2015; Villaros *et al.*, 2018, Couzinié *et al.*, 2021). Either way, the presence of voluminous granite and diatexite at mid-/upper crustal levels requires transfer of granitic magma from lower crustal levels. This process seems to have widely occurred throughout the FMC domain in the Variscan orogen during the Carboniferous, as large volumes of crust–derived granites and diatexites were produced in this region during the Carboniferous (Laurent *et al.*, 2017; Vanderhaeghe *et al.*, 2020).

The process of deep partial melting and extraction of granitic melts typically leaves behind a residual, granulitic lower crust (Clemens 1990; Vielzeuf *et al.*, 1990; White and Powell, 2002; Cawood *et al.*, 2013; Clemens *et al.*, 2020). In the E–FMC, this refractory lower crust is sampled by crustal xenoliths brought up by Cenozoic volcanoes (Leyreloup *et al.*, 1977; Leyreloup, 1992) whose petrology and zircon U–Pb systematics are fully consistent with an origin through extensive melting and melt extraction to form the mid-/upper crustal granites and migmatites (Fig. 15; Vanderhaeghe, 2009; Villaros *et al.*, 2018; Laurent *et al.*, 2023). The metamorphic conditions recorded by the lower crustal xenoliths range from *ca.* 5 kbar and 700 °C to *ca.* 10 kbar and 950 °C (see Leyreloup, 1992; Laurent *et al.*, 2023 and references therein), *i.e.* define a LP-HT metamorphic gradient that perfectly aligns with that recorded by the LGU rocks in the Pontgibaud area. Moreover, these lower crustal rocks underwent granitic melt loss from *ca.* 340 to 310 Ma (Laurent *et al.*, 2023), in agreement with the crystallization ages of the Claveix and Gelles granites (*ca.* 340–320 Ma) obtained here. Altogether, granitic melts that fed the upper-/mid–Crustal plutons and diatexites in the Pontgibaud area were likely generated from a lower crustal source region that underwent a similar metamorphic evolution as that recorded by the granulite xenoliths sampled elsewhere in the E–FMC. Therefore, melt–depleted granulites complementary to the diatexites and granites exposed at the surface likely form the bulk of the lower crust beneath the Pontgibaud area.

The lower crustal granulite xenoliths have chemical and petrographic characteristics consistent with the loss of 25 to 30 vol. per cent melt (Laurent *et al.*, 2023), in agreement with the minimum melt fractions required for efficient melt extraction (20-25 vol. per cent melt; Vigneresse *et al.*, 1996). This requires that the granulitic lower crust represents 2 to 3 times the volume of granitic magma at the present level of exposure. Considering a crustal thickness of *ca.* 28 km in the Pontgibaud area (Zeyen *et al.*, 1997) and a closed-system redistribution of material during Carboniferous melting and granitic magma transport, this entails that the crust consists of a vertical section comprising a 7–14 km-thick upper layer of granite and diatexite (± unmolten country rocks close to the surface), underlain by 14–21 km of refractory migmatite and granulite (Fig. 15). This must be considered as an extreme estimate considering that the upper crust is not entirely formed of liquid extracted from the lower crust.

5 Conclusion

Field observations, metamorphic conditions and geochronological data presented in this study suggests that: 1) the Pontgibaud area exposes a continuous section along a mid–Carboniferous MP to LP/HT metamorphic gradient from micaschists to migmatites, belonging to the Lower Gneiss Unit of the Variscan orogenic crust; 2) this event is followed by the generation and emplacement of crust–derived granitoids represented by the Claveix and Gelles plutons.

Most metamorphic rocks consist of dominantly -meta–sedimentary lithologies with late Edicaran protoliths (maximum deposition ages of *ca.* 590–560 Ma) similar to those documented elsewhere in the FMC for the LGU. These sediments have recorded-P–Tconditions ranging from 2.3–5.3 kbar and 570° to 660°C, dated from 357.6 ± 1.5 to 342.2 ± 4.6 Ma by LA-ICP-MS U–Pb analyses of metamorphic monazite. The contact between the metasedimentary rocks and migmatites is crosscut by peraluminous, cordierite-biotite-bearing Claveix and Gelles granitic plutons dated at 338.0 ± 7.3 Ma and 323.3 ± 9.7 Ma respectively by U–Pb on zircon. Extensive melting and extraction of a large volume of granitic magma from these lithologies requires higher temperature conditions (800°C) than those recorded by the exposed rocks. Accordingly, we propose that the Pontgibaud area is underlain by metamorphic rocks with a similar protolith as the one exposed at the surface, but affected by higher grade metamorphism and magma extraction, which is consistent with the inferred residual nature of granulites sampled by Cenozoic volcanoes. The lower crust is interpreted as a high–grade, residual equivalent of the regionally exposed migmatitic -meta–sedimentary rocks (Leyreloup, 1992; Laurent *et al.*, 2023).

Accordingly, we propose that this segment of the Variscan belt has recorded high temperature metamorphism, deformation, partial melting and melt segregation in an interval between *ca.* 350 Ma to 320 Ma, consistent with propositions where a time gap of 20-30 Ma after crustal thickening and/or increase of the heat flux through the Moho is required to trigger the pervasive melting of the crustal column up to the middle crust (Thompson and Connolly 1995; Vanderhaeghe and Teyssier 2001; Cavalcante *et al.*, 2018). In this scenario, partial melting of the continental crust would be continuous in this 20-30 Ma interval, whereas segregation; accumulation, transport and emplacement of plutons such as Claveix and Gelles represent episodic events dated by U–Pb on zircon at 338 ± 7 Ma et à 323 ± 7 Ma, respectively.

The vertical distribution of lithologies between the upper to lower crust, the latter being ill–defined, may influence the geotherm and therefore the potential for deep geothermal energy production in a given region. Our study has clarified the vertical structure of the Variscan crust in the Pontgibaud area, which will allow to discuss the distribution of heat-producing elements as well as thermal conductivity within the crust column and thus more precisely model the current geotherm (Bellanger *et al.*, 2019).

Acknowledgments

This study has received funding from the ANR (grant GERESFAULT number ANR-19-CE05-0043) and the grant “CNRS IRN FALCoL” to OV and from the CNRS-INSU TelluS-SYSTER program (grant “QuantHyCCO” to OL). The thorough review of four anonymous reviewers helped improve this manuscript.

Supplementary material

Table X. LA-(MC-)ICP-MS U-Pb, trace element and Lu-Hf isotopic analyses on zircon - Metadata.

Table Y. LA-ICP-MS U-Pb isotopic analyses on monazite - Metadata.

The Supplementary Material is available at https://www.bsgf.fr/10.1051/bsgf/2025004/olm.

References

Auzanneau E, Schmidt MW, Vielzeuf D, Connolly JA. 2009. Titanium in phengite: a geobarometer for high temperature eclogites. *Contributions to Mineralogy and Petrology* 159(1): 1. https://doi.org/10.1007/s00410-009-0412-7.

Avigad D, Abbo A, Gerdes A, Schmitt AK. 2022. Crustal evolution of Western Europe: Constraints from detrital zircon U–Pb–Hf–O isotopes. *Gondwana Research* 106: 379–396. https://doi.org/10.1016/J.GR.2022.02.006.

Ballèvre M, Catalán JRM, López-Carmona A, Abati J, Díez-Fernández R, Fernández-Suárez J. 2014. Correlation of the nappe stack in the Ibero-Armorican arc across the Bay of Biscay: A joint French-Spanish project. *Geological Society Special Publication* 405(1): 77–113. https://doi.org/10.1144/SP405.13.

Barbarin B. 1999. A review of the relationships between granitoid types, their origins and their geodynamic environments. *Lithos* 46 (3): 605–626. https://doi.org/10.1016/S0024-4937(98)00085-1.

Barbey P, Marignac C, Montel JM, Macaudière J, Gasquet D, Jabbori J. 1999. Cordierite growth textures and the conditions of genesis and emplacement of crustal granitic magmas: The Velay granite complex (Massif Central, France). *Journal of Petrology* 40(9): 1425–1441. https://doi.org/10.1093/petroj/40.9.1425.

Barbey P, Villaros A, Marignac C, Montel JM. 2015. Multiphase melting, magma emplacement and P–T–time path in late-collisional context: The Velay example (Massif Central, France). *Bulletin de la Société Géologique de France* 186(2–3): 93–116. https://doi.org/10.2113/gssgfbull.186.2-3.93.

Barboza SA, Bergantz GW, Brown M. 1999. Regional granulite facies metamorphism in the Ivrea zone: Is the Mafic Complex the smoking gun or a red herring? *Geology* 27(5): 450.

Bellanger M, Hermant B, Galibert S, Auxiètre JL. 2019. Fault-controlled hydrothermal system associated with major crustal fault zone: future drilling target to assess the deep geothermal potential–The Sioule license project. In: *Proceedings European Geothermal Congress*, Den Haag, The Netherlands

Benmammar A, Couzinié S, Faure M, Cocherie A, Rossi P, Mezger K, Melleton J. 2020. Pressure–temperature conditions and significance of Upper Devonian eclogite and amphibolite facies metamorphisms in southern French Massif Central. *Bulletin de la Société Géologique de France* 191(1). https://doi.org/10.1051/BSGF/2020033.

Berger J, Faure M, Couzinié S, Janots E, Bé Mézème E, Bruguier O, Gèze B, Duguet M. 2024. Short-lived active margin magmatism preceding Variscan collision in the Western French Massif Central. *Bulletin de la Société Géologique de France* 195(1): 7. https://doi.org/10.1051/BSGF/2024003.

Berger J, Féménias O, Ohnenstetter D, Bruguier O, Plissart G, Mercier JC, Demaiffe D. 2010. New occurrence of UHP eclogites in Limousin (French Massif Central): Age, tectonic setting and fluid–rock interactions. *Lithos* 118(3): 365–382. https://doi.org/10.1016/j.lithos.2010.05.013.

Bernard-Griffiths J, Cornichet J. 1985. Origin of eclogites from South Brittany, France: A Sm–Nd isotopic and REE study. *Chemical Geology: Isotope Geoscience Section* 52(2): 185–201. https://doi.org/10.1016/0168-9622(85)90017-X.

Bertrand JM, Leterrier J, Cuney M, Brouand M, Stussi JM, Delaperrière E. 2001. Géochronologie U–Pb sur zircons de granitoïdes du Confolentais, du massif de Charroux–Civray (seuil du Poitou) et de Vendée. *Géologie de la France* 1(2): 167–189.

Binon M, Pin C. 1989. Géochronologie Rb–Sr et U–Pb des granites du Mayet-de-Montagne et des Bois Noirs, Montagne Bourbonnaise (Massif Central). *Bulletin de la Société Géologique de France* V (4): 695–703. https://doi.org/10.2113/GSSGFBULL.V.4.695.

Bouilhol P, Leyreloup AF, Delor C, Vauchez A, Monié P. 2006. Relationships between lower and upper crust tectonic during doming: the mylonitic southern edge of the Velay metamorphic core complex (Cévennes, French Massif Central). *Geodinamica Acta* 19(3–4): 137–153. https://doi.org/10.3166/GA.19.137-153.

Bouvier A, Vervoort JD, Patchett PJ. 2008. The Lu–Hf and Sm–Nd isotopic composition of CHUR: Constraints from unequilibrated chondrites and implications for the bulk composition of terrestrial planets. *Earth and Planetary Science Letters* 273(1–2): 48–57. https://doi.org/10.1016/J.EPSL.2008.06.010.

Brodie KH, Rutter EH, Evans P. 1982. On the structure of the Ivrea–Verbano Zone (northern Italy) and its implications for present-day lower continental crust geometry. *Terra Nova* 4(1): 34–40.

Brousse R, 1990. Carte géologique de la France à 1/50 000. 740, La Tour-d'Auvergne, BRGM (French Geological Survey). Bureau de recherches géologiques et minières'.

Brown M. 2001. Crustal melting and granite magmatism: key issues. *Physics and Chemistry of the Earth, Part A: Solid Earth and Geodesy* 26(4): 201–212. https://doi.org/10.1016/S1464-1895(01)00047-3.

Burg JP, Leyreloup AF, Romney F, Delor CP. 1989. Inverted metamorphic zonation and Variscan thrust tectonics in the Rouergue area (Massif Central, France): P–T–t record from mineral to regional scale. *Geological Society Special Publication* 43: 423–439. https://doi.org/10.1144/GSL.SP.1989.043.01.38.

Burg JP, Matte P, Leyreloup A, Marchand J. 1984. Inverted metamorphic zonation and large-scale thrusting in the Variscan Belt: An example in the French Massif Central. *Geological Society Special Publication* 14: 47–61. https://doi.org/10.1144/GSL.SP.1984.014.01.05.

Burg JP, Matte PJ. 1978. A cross section through the French Massif Central and the scope of its Variscan geodynamic evolution. *Zeitschrift der Deutschen Geologischen Gesellschaft* 129(2): 429–460. https://doi.org/10.1127/zdgg/129/1978/429.

Burg JP, Vanderhaeghe O. 1993. Structures and way-up criteria in migmatites, with application to the Velay dome (French Massif Central). *Journal of Structural Geology* 15(11): 1293–1301. https://doi.org/10.1016/0191-8141(93)90103-H.

Cavalcante C, Hollanda MH, Vauchez A, Kawata M. 2018. How long can the middle crust remain partially molten during orogeny? *Geology* 46(10): 839–842. https://doi.org/10.1130/G45126.1.

Cawood PA, Hawkesworth CJ, Dhuime B. 2013. The continental record and the generation of continental crust. *Bulletin of the Geological Society of America* 125(1–2): 14–32. https://doi.org/10.1130/B30722.1.

Chantraine J, Autran A, Cavelier C, Clozier L. 2003. Carte géologique de la France à l'échelle du millionième. Bureau de recherches géologiques et minières'.

Chelle-Michou C, Faure M, Cocherie A, Rossi P, Paquette JL, Ganne J. 2017. Pre-Cadomian to late-Variscan odyssey of the eastern Massif Central, France: Formation of the West European crust in a nutshell. *Gondwana Research* 46: 170–190. https://doi.org/10.1016/j.gr.2017.02.010.

Chu NC, Taylor RN, Chavagnac V, Nesbitt RW, Boella RM, Milton JA. 2002. Hf isotope ratio analysis using multi-collector inductively coupled plasma mass spectrometry: an evaluation of isobaric interference corrections. *Journal of Analytical Atomic*

Spectrometry 17(12): 1567–1574. https://doi.org/10.1039/B206707B.

Clemens JD. 1990. The granulite–granite connexion. In: *Granulites and crustal evolution*, pp. 25–36. https://doi.org/10.1007/978-94-009-2055-2_3/COVER.

Clemens JD, Stevens G, Bryan SE. 2020. Conditions during the formation of granitic magmas by crustal melting– Hot or cold; drenched, damp or dry? *Earth-Science Reviews* 200: 102982. https://doi.org/10.1016/J.EARSCIREV.2019.102982.

Coggon R, Holland TJB. 2002. Mixing properties of phengitic micas and revised garnet–phengite thermobarometers. *Journal of Metamorphic Geology* 20(7): 683–696. https://doi.org/10.1046/j.1525-1314.2002.00395.x.

Connolly JAD. 2009. The geodynamic equation of state: What and how. *Geochemistry, Geophysics, Geosystems* 10(10): 10014. https://doi.org/10.1029/2009GC002540.

Costa S, Rey P. 1995. Lower crustal rejuvenation and growth during post-thickening collapse: Insights from a crustal cross section through a Variscan metamorphic core complex. *Geology* 23(10): 905–908. https://doi.org/10.1130/0091-7613(1995)0230905:LCRAGD2.3.CO;2–.

Do Couto D, Faure M, Augier R, Cocherie A, Rossi P, Li XH, Lin W. 2016. Monazite U–Th–Pb EPMA and zircon U–Pb SIMS chronological constraints on the tectonic, metamorphic, and thermal events in the inner part of the Variscan orogen, example from the Sioule series, French Massif Central. *International Journal of Earth Sciences* 105(2): 557–579. https://doi.org/10.1007/s00531-015-1184-0.

Couzinié S. *et al.*, 2017. Cadomian S-type granites as basement rocks of the Variscan belt (Massif Central, France): implications for the crustal evolution of the north Gondwana margin. Lithos 286–287: 16–34

Couzinié S, Laurent O, Bouilhol P, Marko L, Moyen JF. 2021. When zircon drowns: Elusive geochronological record of water-fluxed orthogneiss melting in the Velay dome (Massif Central, France). *Lithos* 384–385: 105938. https://doi.org/10.1016/j.lithos.2020.105938.

Couzinié S, Laurent O, Chelle-Michou C, Bouilhol P, Paquette JL, Gannoun AM, Moyen JF. 2019. Detrital zircon U–Pb–Hf systematics of Ediacaran metasediments from the French Massif Central: Consequences for the crustal evolution of the north Gondwana margin. *Precambrian Research* 324: 269–284. https://doi.org/10.1016/j.precamres.2019.01.016.

Couzinié S, Bouilhol P, Laurent O, Moyen JF, Villaros A. 2016. Post-collisional magmatism: Crustal growth not identified by zircon Hf–O isotopes. *Earth and Planetary Science Letters* 456: 182–195. https://doi.org/10.1016/j.epsl.2016.09.033.

Demarchi G, Quick JE, Sinigoi S, Mayer A. 1998. Pressure gradient and original orientation of a lower-crustal intrusion in the Ivrea–Verbano Zone, Northern Italy. *Journal name missing*, volume (issue): page range. [DOI if available[pg1]].

Dostal J, Dupuy C, Leyreloup A. 1980. Geochemistry and petrology of meta-igneous granulitic xenoliths in Neogene volcanic rocks of the Massif Central, France — implications for the lower crust. *Earth and Planetary Science Letters* 50(1): 31–40. https://doi.org/10.1016/0012-821X(80)90117-X

Downes H, Leyreloup A. 1986. Granulitic xenoliths from the French Massif Central: petrology, Sr and Nd isotope systematics and model age estimates. *Geological Society Special Publication* 24: 319–330. https://doi.org/10.1144/GSL.SP.1986.024.01.28.

Duwiquet H, Arbaret L, Guillou-Frottier L, Heap MJ, Bellanger M. 2019. On the geothermal potential of crustal fault zones: a case study from the Pontgibaud area (French Massif Central, France). *Geothermal Energy* 7(1). https://doi.org/10.1186/s40517-019-0150-7.

Duwiquet H, Guillou-Frottier L, Arbaret L, Bellanger M, Guillon T, Heap MJ. 2021. Crustal fault zones (CFZ) as geothermal power systems: a preliminary 3D THM model constrained by a multidisciplinary approach. *Geofluids* 2021. https://doi.org/10.1155/2021/8855632.

England PC, Thompson AB. 1984. Pressure–temperature–time paths of regional metamorphism I. Heat transfer during the evolution of regions of thickened continental crust. *Journal of Petrology* 25(4): 894–928. https://doi.org/10.1093/petrology/25.4.894—

Faure M, Bé Mézème E, Cocherie A, Rossi P, Chemenda A, Boutelier D. 2008. Devonian geodynamic evolution of the Variscan Belt, insights from the French Massif Central and Massif Armoricain. *Tectonics* 27(2). https://doi.org/10.1029/2007TC002115.

Faure M, Lardeaux J, Ledru P. 2009. A review of the pre-Permian geology of the Variscan French Massif Central. *Comptes Rendus Géoscience* 341(2–3): 202–213. https://doi.org/10.1016/j.crte.2008.12.001.

Fernandez A. 1969. La série cristallophyllienne et les granites de la région de Pontgibaud (Puy de Dôme), Massif Central Français. Doctoral dissertation, Université de Clermont-Ferrand.

Fernandez A, Tempier P. 1977. Mise en place, fabrique mésoscopique et rapports structuraux du granite de Gelles avec l'enveloppe métamorphique (Puy-de-Dôme, Massif Central français). *Bulletin du B.R.G.M.* (2), IV(4): 357–366.

Finger E, Roberts MP, Haunschmid B, Schermaier A, Steyrer HP. 1997. Variscan granitoids of Central Europe: their typology, potential sources and tectonothermal relations. *Mineralogy and Petrology* 61(1–4): 67–96.

Gardien V, Tegyey M, Lardeaux JM, Misseri M, Dufour E. 1990. Crust–mantle relationships in the French Variscan chain: the example of the Southern Monts du Lyonnais unit (eastern French Massif Central). *Journal of Metamorphic Geology* 8(5): 477–492. https://doi.org/10.1111/J.1525-1314.1990.TB00481.X.

Gardien V, Vanderhaeghe O, Arnaud N, Cocherie A, Grange M, Lécuyer C. 2011. Thermal maturation and exhumation of a middle orogenic crust in the Livradois area (French Massif Central). *Bulletin de la Société Géologique de France* 182(1): 5–24. https://doi.org/10.2113/gssgfbull.182.1.5.

Gasquet D, Boulvais P, 2010. Miocene to Messinian deformation and hydrothermal activity in a pre-Alpine basement massif of the French Western Alps: new U–Th–Pb and Argon ages from the Lauzière Massif. *Bulletin de la Société Géologique de France* 181: 227–241. https://doi.org/10.2113/gssgfbull.181.3.227.

Girardeau J, Dubuisson G, Mercier JC. 1986. Cinématique de mise en place des ophiolites et nappes cristallophylliennes du Limousin, Ouest du Massif Central français. *Bulletin de la Société Géologique de France* II(5): 849–860. https://doi.org/10.2113/GSSGFBULL.II.5.849.

Guergouz C, Martin L, Vanderhaeghe O, Thébaud N, Fiorentini M. 2018. Zircon and monazite petrochronologic record of prolonged amphibolite to granulite facies metamorphism in the Ivrea–Verbano and Strona–Ceneri Zones, NW Italy. *Lithos* 308–309: 1–18. https://doi.org/10.1016/j.lithos.2018.02.014.

Guille BT, Olivier P, Paquette JL, Bosse V, Guillaume D. 2019. Evolution of the middle crust of the Pyrenees during the Paleozoic: new data on the plutonic rocks from the North Pyrenean Agly

Massif. *International Journal of Earth Sciences* 108(1): 245–265. https://doi.org/10.1007/S00531-018-1652-4.

Hacker BR, Kelemen PB, Behn MD. 2011. Differentiation of the continental crust by relamination. *Earth and Planetary Science Letters* 307(3–4): 501–516. https://doi.org/10.1016/j.epsl.2011.05.024.

Handy MR, Franz L, Heller F, Janott B, Zurbriggen R. 1999. Multistage accretion and exhumation of the continental crust (Ivrea crustal section, Italy and Switzerland). *Tectonics* 18(6): 1154–1177. https://doi.org/10.1029/1999TC900034.

Hawkesworth CJ, Dhuime B, Pietranik AB, Cawood PA, Kemp AIS, Storey CD. 2010. The generation and evolution of the continental crust. *Journal of the Geological Society* 167(2): 229–248. https://doi.org/10.1144/0016-76492009-072.

Hellstrom J, Paton C, Woodhead J, Hergt J. 2008. Iolite: software for spatially resolved LA-(quad and MC) ICP-MS analysis. *Mineralogical Association of Canada Short Course Series* 40: 343–348.

Henk A, von Blanckenburg F, Finger F, Schaltegger U, Zulauf G. 2000. Syn-convergent high-temperature metamorphism and magmatism in the Variscides: a discussion of potential heat sources. *Geological Society Special Publication* 179: 387–399. https://doi.org/10.1144/GSL.SP.2000.179.01.23.

Holdaway MJ. 2001. Recalibration of the GASP geobarometer in light of recent garnet and plagioclase activity models and versions of the garnet–biotite geothermometer. *American Mineralogist* 86 (10): 1117–1129.

Holland T, Baker J, Powell R. 1998. Mixing properties and activity–composition relationships of chlorites in the system MgO–FeO–Al_2O_3–SiO_2–H_2O. *European Journal of Mineralogy* 10(3): 395–406. https://doi.org/10.1127/ejm/10/3/0395.

Holland T, Powell R. 1996. Thermodynamics of order–disorder in minerals: II. Symmetric formalism applied to solid solutions. *American Mineralogist* 81(11–12): 1425–1437. https://doi.org/10.2138/am-1996-11-1215.

Holland T, Powell R. 2003. Activity–composition relations for phases in petrological calculations: an asymmetric multicomponent formulation. *Contributions to Mineralogy and Petrology* 145(4): 492–501. https://doi.org/10.1007/S00410-003-0464-Z.

Holland T, Powell R. 2011. An improved and extended internally consistent thermodynamic dataset for phases of petrological interest, involving a new equation of state for solids. *Journal of Metamorphic Geology* 29(3): 333–383. https://doi.org/10.1111/J.1525-1314.2010.00923.X.

Horstwood M, 2016. Community-derived standards for LA-ICP-MS U–Th–Pb geochronology– uncertainty propagation, age interpretation and data reporting. *Geostandards and Geoanalytical Research* 40: n/a. https://doi.org/10.1111/j.1751-908X.2016.00379.x.

Hottin AM, Camus G, Besson JC, Michaely B, Marchand J, Perichaud JJ. 1989. Notice explicative de la feuille Pontgibaud à 1/50 000.

Jacob JB, 2021. Crustal melting vs. fractionation of basaltic magmas: Part 2, Attempting to quantify mantle and crustal contributions in granitoids. *Lithos* 402–403: 106292. https://doi.org/10.1016/J.LITHOS.2021.106292.

Janoušek V, Bowes DR, Rogers G, Farrow CM, Jelínek E. 2000. Modelling diverse processes in the petrogenesis of a composite batholith: the Central Bohemian Pluton, Central European Hercynides. *Journal of Petrology* 41(4): 511–543. https://doi.org/10.1093/PETROLOGY/41.4.511.

Kelsey DE, Clark C, Hand M. 2008. Thermobarometric modelling of zircon and monazite growth in melt-bearing systems: Examples using model metapelitic and metapsammitic granulites. *Journal of Metamorphic Geology* 26(2): 199–212. https://doi.org/10.1111/j.1525-1314.2007.00757.x.

Kennedy A, Wotzlaw JF, Crowley J, Schmitz M, Schaltegger U. 2014. Eocene zircon reference material for microanalysis of U–Th–Pb isotopes and trace elements. *The Canadian Mineralogist* 52: 409–421. https://doi.org/10.3749/canmin.52.3.409.

Lardeaux JM, 2014. The Moldanubian Zone in the French Massif Central, Vosges/Schwarzwald and Bohemian Massif revisited: Differences and similarities. *Geological Society Special Publication* 405(1): 7–44. https://doi.org/10.1144/SP405.14.

Lardeaux JM, Ledru P, Daniel I, Duchene S. 2001. The Variscan French Massif Central– A new addition to the ultra-high pressure metamorphic "club": Exhumation processes and geodynamic consequences. *Tectonophysics* 332(1–2): 143–155. https://doi.org/10.1016/S0040-1951(00)00253-5"".

Laurent O, 2017. Protracted, coeval crust and mantle melting during Variscan late-orogenic evolution: U–Pb dating in the eastern French Massif Central. *International Journal of Earth Sciences* 106(2): 421–451. https://doi.org/10.1007/s00531-016-1434-9.

Laurent O, Couzinié S, Doucet LS. 2023. Timescales of ultra-high temperature metamorphism and crustal differentiation: Zircon petrochronology from granulite xenoliths of the Variscan French Massif Central. *Earth and Planetary Science Letters* 611: 118133. https://doi.org/10.1016/J.EPSL.2023.118133.

Ledru P, 1989. Où sont les nappes dans le Massif Central français? *Bulletin de la Société Géologique de France* V(3): 605–618. https://doi.org/10.2113/gssgfbull.V.3.605.

Ledru P, Courrioux G, Dallain C, Lardeaux JM, Montel JM, Vanderhaeghe O, Vitel G. 2001. The Velay dome (French Massif Central): melt generation and granite emplacement during orogenic evolution. *Tectonophysics* 342(3–4): 207–237.

Leyreloup A. 1992. La croûte métamorphique du Sud de la France (Massif Central, Languedoc). Géologie de surface et des enclaves remontées par les volcans cénozoïques: Le rôle des intrusions mafiques basi-crustales dans la croûte inférieure. (Thèse d'État). Montpellier.

Leyreloup A, Dupuy C, Andriambololona R. 1977. Catazonal xenoliths in French Neogene volcanic rocks: constitution of the lower crust 2. Chemical composition and consequences of the evolution of the French Massif Central Precambrian crust. *Contributions to Mineralogy and Petrology* 62(3): 283–300.

Lotout C, Pitra P, Poujol M, Anczkiewicz R, Van Den Driessche J. 2018. Timing and duration of Variscan high-pressure metamorphism in the French Massif Central: A multimethod geochronological study from the Najac Massif. *Lithos* 308–309: 381–394. https://doi.org/10.1016/j.lithos.2018.03.022.

Lotout C, Poujol M, Pitra P, Anczkiewicz R, Van Den Driessche J. 2020. From burial to exhumation: emplacement and metamorphism of mafic eclogitic terranes constrained through multimethod petrochronology, case study from the Lévézou Massif (French Massif Central, Variscan Belt). *Journal of Petrology* 61(4). https://doi.org/10.1093/petrology/egaa046.

Marsh JH, Jørgensen TRC, Petrus JA, Hamilton MA, Mole DR. 2019. U–Pb, trace element, and hafnium isotope composition of the

Maniitsoq zircon: A potential new Archean zircon reference material. *Goldschmidt Abstracts*: 2161.

Matte P. 1986. Tectonics and plate tectonics model for the Variscan belt of Europe. *Tectonophysics* 126(2–4): 329–374. https://doi.org/10.1016/0040-1951(86)90237-4.

Matte P. 2001. The Variscan collage [pg2]and orogeny (480–290 Ma) and the tectonic definition of the Armorica microplate: A review. *Terra Nova* 13: 122–128.

Melleton J, Cocherie A, Faure M, Rossi P. 2010. Precambrian protoliths and Early Paleozoic magmatism in the French Massif Central: U–Pb data and the North Gondwana connection in the West European Variscan Belt. *Gondwana Research* 17(1): 13–25. https://doi.org/10.1016/j.gr.2009.05.007.

Monnier L, 2021. Episodic precipitation of wolframite during an orogen: The Echassières District, Variscan Belt of France. *Minerals* 11(9): 923. https://doi.org/10.3390/MIN11090923.

Montel JM, Vielzeuf D. 1997. Partial melting of metagreywackes, part II. Compositions of minerals and melts. *Contributions to Mineralogy and Petrology* 128(2): 176–196.

Morel MLA, Nebel O, Nebel-Jacobsen YJ, Miller JS, Vroon PZ. 2008. Hafnium isotope characterization of the GJ-1 zircon reference material by solution and laser-ablation MC-ICP-MS. *Chemical Geology* 255(1–2): 231–235. https://doi.org/10.1016/J.CHEMGEO.2008.06.040.

Mougeot R, Respaut JP, Ledru P, Marignac C. 1997. U–Pb chronology on accessory minerals of the Velay anatectic dome (French Massif Central). *European Journal of Mineralogy* 9(1): 141–156.

Moyen JF, 2017. Collision vs. subduction-related magmatism: Two contrasting ways of granite formation and implications for crustal growth. *Lithos* 277: 154–177. https://doi.org/10.1016/j.lithos.2016.09.018.

Négroni JM. 1981. Le district de Pontgibaud: cadre géologique, évolution structurale et métallogénique. Doctoral dissertation, Université de Clermont-Ferrand.

Newton RC, Charlu TV, Kleppa OJ. 1980. Thermochemistry of the high structural state plagioclases. *Geochimica et Cosmochimica Acta* 44(7): 933–941. https://doi.org/10.1016/0016-7037(80)90283-5.

Olivier P, Gleizes G, Paquette JL, Sáez CM. 2008. Structure and U–Pb dating of the Saint-Arnac pluton and the Ansignan charnockite (Agly Massif): a cross-section from the upper to the middle crust of the Variscan Eastern Pyrenees. *Journal of the Geological Society* 165(1): 141–152. https://doi.org/10.1144/0016-76492006-185.

Paquette JL, Tiepolo M. 2007. High resolution (5 µm) U–Th–Pb isotope dating of monazite with excimer laser ablation (ELA)-ICP-MS. *Chemical Geology* 240(3): 222–237. https://doi.org/10.1016/j.chemgeo.2007.02.014.

Paton C, Woodhead J, Hellstrom J, Hergt J, Greig A, Maas R. 2010. Improved laser ablation U–Pb zircon geochronology through robust downhole fractionation correction. *Geochemistry, Geophysics, Geosystems* 11: Q0AA06. https://doi.org/10.1029/2009GC002618.

Petrus JA, Kamber BS. 2012. VizualAge: A novel approach to laser ablation ICP-MS U–Pb geochronology data reduction. *Geostandards and Geoanalytical Research* 36(3): 247–270. https://doi.org/10.1111/J.1751-908X.2012.00158.X.

Pin C, Lancelot J. 1982. U–Pb dating of an early Paleozoic bimodal magmatism in the French Massif Central and of its further metamorphic evolution. *Contributions to Mineralogy and Petrology* 79(1): 1–12. https://doi.org/10.1007/BF00376956.

Pin C, Paquette JL. 2002. Le magmatisme basique calcoalcalin d'âge dévono-dinantien du nord du Massif Central, témoin d'une marge active hercynienne: arguments géochimiques et isotopiques Sr/Nd. *Geodinamica Acta* 15(1): 63–77. https://doi.org/10.1080/09853111.2002.10510739".

von Raumer JF, Finger F, Veselá P, Stampfli GM. 2014. Durbachites–Vaugnerites: a geodynamic marker in the Central European Variscan orogen. *Terra Nova* 26(2): 85–95. https://doi.org/10.1111/ter.12071.

Rubatto D, Williams IS, Buick IS. 2001. Zircon and monazite response to prograde metamorphism in the Reynolds Range, central Australia. *Contributions to Mineralogy and Petrology* 140(4): 458–468. https://doi.org/10.1007/PL00007673.

Rudnick RL. 1995. Making continental crust. *Nature* 378(6557): 571–578. https://doi.org/10.1038/378571a0.

Sandiford M, McLaren S, Neumann N. 2002. Long-term thermal consequences of the redistribution of heat-producing elements associated with large-scale granitic complexes. *Journal of Metamorphic Geology* 20(1): 87–98. https://doi.org/10.1046/J.0263-4929.2001.00359.X.

Santallier D, Briand B, Menot R, Piboule M. 1988. Les complexes leptyno-amphiboliques (C.L.A.): revue critique et suggestions pour un meilleur emploi de ce terme. *Bulletin de la Société Géologique de France* IV(1): 3–12. https://doi.org/10.2113/gssgfbull.IV.1.3.

Santallier D, Lardeaux J, Marchand J, Marignac C. 1994. Metamorphism. In: Chantraine J, Rolet J, Santallier DS, Piqué A, Keppie JD, eds. *Pre-Mesozoic Geology in France and Related Areas*. Berlin: Springer, pp. 324–340. https://doi.org/10.1007.

Sawyer EW, Cesare B, Brown M. 2011. When the continental crust melts. *Elements* 7(4): 229–234. https://doi.org/10.2113/GSELEMENTS.7.4.229.

Scherer E, Münker C, Mezger K. 2001. Calibration of the lutetium–hafnium clock. *Science* 293(5530): 683–687. https://doi.org/10.1126/SCIENCE.1061372.

Schulz B. 2009. EMP-monazite age controls on P–T paths of garnet metapelites in the Variscan inverted metamorphic sequence of La Sioule, French Massif Central. *Bulletin de la Société Géologique de France* 180(3): 271–282. https://doi.org/10.2113/gssgfbull.180.3.271.

Schulz B. 2014. Early Carboniferous P–T path from the Upper Gneiss Unit of Haut-Allier (French Massif Central)– Reconstructed by geothermobarometry and EMP–Th–U–Pb monazite dating. *Journal of Geosciences (Czech Republic)* 59(4): 327–349. https://doi.org/10.3190/jgeosci.178.

Schulz B, Triboulet C, Audren C, Feybesse JL. 1996. Zoned garnets in metapelites and P–T–deformation path interpretation of the Variscan inverted metamorphic sequence of Haut-Allier, French Massif Central. *Zeitschrift der Deutschen Geologischen Gesellschaft* 147(2): 249–273. https://doi.org/10.1127/zdgg/147/1996/249.

Shaw A, Downes H, Thirlwall MF. 1993. The quartz–diorites of Limousin: elemental and isotopic evidence for Devono–Carboniferous subduction in the Hercynian belt of the French Massif Central. *Chemical Geology* 107(1–2): 1–18. https://doi.org/10.1016/0009-2541(93)90098-4.

Sláma J, 2008. Plešovice zircon — A new natural reference material for U–Pb and Hf isotopic microanalysis. *Chemical Geology* 249(1): 1–35. https://doi.org/10.1016/j.chemgeo.2007.11.005.

Spencer CJ, Kirkland CL, Taylor RJM. 2016. Strategies towards statistically robust interpretations of in situ U–Pb zircon geochronology. *Geoscience Frontiers* 7(4): 581–589. https://doi.org/10.1016/j.gsf.2015.11.006.

Tajčmanová L, Connolly JAD, Cesare B. 2009. A thermodynamic model for titanium and ferric iron solution in biotite. *Journal of Metamorphic Geology* 27(2): 153–165. https://doi.org/10.1111/J.1525-1314.2009.00812.X.

Tempier P. 1969. Hypothèse sur une relation possible entre les séries cristallophylliennes de la Moyenne Dordogne et de Pontgibaud. *Comptes Rendus de l'Académie des Sciences, Paris*: 1–4.

Tempier P. 1974. Les schistes cristallins de la région de Bourg-Lastic (Puy-de-Dôme). Étude pétrographique et structurale. *Revue des Sciences Naturelles d'Auvergne* 40: 3–25.

Thompson AB, Connolly JAD. 1995. Melting of the continental crust: some thermal and petrological constraints on anatexis in continental collision zones and other tectonic settings. *Journal of Geophysical Research* 100(B8). https://doi.org/10.1029/95jb00191.

Vanderhaeghe O. 2009. Migmatites, granites and orogeny: flow modes of partially-molten rocks and magmas associated with melt/solid segregation in orogenic belts. *Tectonophysics* 477(3): 119–134. https://doi.org/10.1016/j.tecto.2009.06.021.

Vanderhaeghe O, 2020. Flow of partially molten crust controlling construction, growth and collapse of the Variscan orogenic belt: the geologic record of the French Massif Central. *BSGF - Earth Sciences Bulletin* 191. https://doi.org/10.1051/bsgf/2020013.

Vanderhaeghe O, Teyssier C. 2001. Partial melting and flow of orogens. *Tectonophysics* 342(3–4): 451–472. https://doi.org/10.1016/S0040-1951(01)00175-5.

Vermeesch P. 2018. IsoplotR: a free and open toolbox for geochronology. *Geoscience Frontiers* 9(5): 1479–1493. https://doi.org/10.1016/j.gsf.2018.04.001.

Vielzeuf D. 1996. Les massifs nord-pyrénéens à soubassement granulitique. In: Barnolas A, Chiron JC, eds. *Synthèse géologique et géophysique des Pyrénées*. BRGM–ITGE: 502–521.

Vielzeuf D, Clemens JD, Pin C, Moinet E. 1990. Granites, granulites, and crustal differentiation. In: *Granulites and crustal evolution*: 59–85. https://doi.org/10.1007/978-94-009-2055-2_5/COVER.

Vielzeuf D, Paquette JL, Clemens JD, Stevens G, Gannoun A, Suchorski K, Saúl A. 2021. Age, duration and mineral markers of magma interactions in the deep crust: an example from the Pyrenees. *Contributions to Mineralogy and Petrology* 176(5): 1–22. https://doi.org/10.1007/S00410-021-01789-2.

Vigneresse JL, Barbey P, Cuney M. 1996. Rheological transitions during partial melting and crystallization with application to felsic magma segregation and transfer. *Journal of Petrology* 37(6): 1579–1600.

Villaros A, Laurent O, Couzinié S, Moyen JF, Mintrone M. 2018. Plutons and domes: the consequences of anatectic magma extraction — example from the southeastern French Massif Central. *International Journal of Earth Sciences* 107(8): 2819–2842. https://doi.org/10.1007/s00531-018-1630-x.

Waldbaum DR, Thompson JB. 1968. Mixing properties of sanidine crystalline solutions: II. Calculations based on volume data. *American Mineralogist* 53(11–12): 2000–2017.

Wendt I, Carl C. 1991. The statistical distribution of the mean squared weighted deviation. *Chemical Geology: Isotope Geoscience Section* 86(4): 275–285. https://doi.org/10.1016/0168-9622(91)90010-T.

Werle M, Stevens G, Moyen J, Laurent O, Harris C, Lana CC, Janney PE. 2023. Cryptic crustal growth identified through Variscan post-collisional lamprophyre–granite composite dykes, French Massif Central. *Lithos* 454: 107270.

White RW, Powell R, Holland T, Worley B. 2000. The effect of TiO_2 and Fe_2O_3 on metapelitic assemblages at greenschist and amphibolite facies conditions: mineral equilibria calculations in the system $K_2O–FeO–MgO–Al_2O_3–SiO_2–H_2O–TiO_2–Fe_2O_3$. *Journal of Metamorphic Geology* 18(5): 497–511. https://doi.org/10.1046/j.1525-1314.2000.00269.x.

White RW, Powell R. 2002. Melt loss and the preservation of granulite facies mineral assemblages. Journal of Metamorphic Geology 20(7): 621–632. https://doi.org/10.1046/J.1525-1314.2002.00206_20_7.X.

White RW, Powell R, Holland T. 2001. Calculation of partial melting equilibria in the system $Na_2O–CaO–K_2O–FeO–MgO–Al_2O_3–SiO_2–H_2O$ (NCKFMASH). Journal of Metamorphic Geology 19(2): 139–153. https://doi.org/10.1046/j.0263-4929.2000.00303.x.—

Wiedenbeck M, 1995. Three natural zircon standards for U–Th–Pb, Lu–Hf, trace element and REE analyses. Geostandards Newsletter 19: 1–23. https://doi.org/10.1111/j.1751-908X.1995.tb00147.x.

Woodhead JD, Hergt JM. 2005. A preliminary appraisal of seven natural zircon reference materials for in situ Hf isotope determination. Geostandards and Geoanalytical Research 29(2): 183–195. https://doi.org/10.1111/J.1751-908X.2005.TB00891.X.

Yakymchuk C, Brown M. 2014. Behaviour of zircon and monazite during crustal melting. Journal of the Geological Society 171(4): 465–479. https://doi.org/10.1144/jgs2013-115.

Zeyen H, Novak O, Landes M, Prodehl C, Driad L, Hirn A. 1997. Refraction-s N–S seismic investigations of the northern Massif Central (France). Tectonophysics 275(1–3): 99–117. https://doi.org/10.1016/S0040-1951(97)00017-6.

Zingg A, Handy MR, Hunziker JC, Schmid SM. 1990. Tectonometamorphic history of the Ivrea Zone and its relationship to the crustal evolution of the Southern Alps. Tectonophysics 182(1–2): 169–192. https://doi.org/10.1016/0040-1951(90)90349-D.

Cite this article as: do Carmo C, Vanderhaeghe O, Laurent O, Berger J, Bellanger M, Leisen M, Chmeleff J. 2025. Petrogenetic link between metasedimentary rocks, migmatites and granitoids in the Variscan basement of the Pontgibaud area, French Massif Central– implications for the crustal structure, *BSGF - Earth Sciences Bulletin* 196: 13. https://doi.org/10.1051/bsgf/2025004